THESIS FOR THE DEGREE OF LICENTIATE OF ENGINEERING

Water signatures from Ganymede's atmosphere

Preparing the observations for ESA's JUICE Mission

Teresa Margheri

CHALMERS
UNIVERSITY OF TECHNOLOGY

Department of Space, Earth and Environment
Chalmers University of Technology
Gothenburg, Sweden, 2025

Water signatures from Ganymede's atmosphere

Teresa Margheri

Front cover image: Artistic Illustration.
Credit: NASA/Goddard Space Flight Center.

This thesis has been prepared using LaTeX.
Department of Space, Earth and Environment
Chalmers University of Technology
SE-412 96 Gothenburg, Sweden
Phone: +46 (0)31 772 1000
www.chalmers.se

Printed by Chalmers Reproservice
Gothenburg, Sweden, September 2025

To those who dare to fly higher,
and seek the vastness of the universe.

— Inspired by Jonathan Livingston — Richard Bach

Abstract

The icy Galilean moons and their potential subsurface oceans are candidates for habitable environments in the Solar System, but still remain largely unexplored. Their tenuous atmospheres are expected to be dominated by water, with enhanced abundance in regions where surface ice sublimates, and may be further enriched by plumes of volatile material escaping through cracks in the ice shell. The Submillimeter Wave Instrument (SWI) onboard ESA's JUICE mission, launched in 2023, is designed to study rotational water lines in the exospheres of the icy Galilean moons.

This thesis focuses on assessing the feasibility of detecting water plumes on Ganymede, the largest moon of Jupiter, and optimizing observational strategies for SWI. The 3D non-LTE radiative transfer code LIME was employed to simulate water spectral line profiles and study how their profiles change by varying plume parameters such as temperature, production rate, and velocity fields. Various observation geometries were tested to account for the planned moon-monitoring phase of SWI, approximately 1.2 million km from Ganymede.

The results demonstrate that SWI can detect plumes with production rates as low as 10^{27} s^{-1} under favorable geometries, particularly when the plume is located at the limb of Ganymede. Temperature variations affect the emission signal, while velocity fields introduce distinctive Doppler shifts and line broadening that could serve as diagnostics of plume dynamics. Finally, the thesis discusses the limitations of the current models and outlines future work, including the exploration of lower plume temperatures, more realistic plume dynamics, and additional water transitions and collisional partners. Extending this approach to Europa and Callisto will further enhance the scientific return of JUICE and deepen our understanding of water in the Jovian system.

Keywords: Planets and satellites atmospheres, submillimeter instrument, Ganymede, radiative transfer, space vehicles

List of Publications

This thesis is based on the following publications:

[A] **T. Margheri**, E.S. Wirström, P. Bjerkeli, L. Rezac, P. Hartogh, "Radiative Transfer Models of Water Plumes in Ganymede's Atmosphere. Preparing SWI/JUICE Observations.". Submitted to Astronomy & Astrophysics (A&A), June 2025.

Acknowledgments

This journey has been filled with the support and kindness of many wonderful people, and I apologize if I cannot mention everyone by name. I will start by expressing my deepest gratitude to Eva, my supervisor, for her unwavering presence, patience, dedication, and kindness. She has guided me with care, always brightened my working days with her great smile, and filled them with joy and laughter. I could not imagine a more supportive mentor to continue this path with. I am extremely thankful to Per, my supervisor, whose caring and encouraging presence makes this journey brighter. His creativity, problem-solving spirit, and curiosity inspire me to grow not only as a scientist but also as a person. I would like to thank Wouter, my examiner, whose wisdom and kind guidance have helped me on many occasions, whether in exploring important and challenging concepts with enthusiasm and curiosity, trusting me to assist him as his assistant teacher, or reviewing my thesis with care. My gratitude also goes to Matthias, my line manager, for helping me see challenges as opportunities and for reminding me that vulnerability can be your greatest strength. His empathy and support have meant so much to me. He has encouraged me to grow as a person and has been a guiding light in moments of doubt and discouragement. To Robert, for his creativity and human sensitivity. To all my colleagues for their support and for creating a friendly and inspiring work environment. To Sara, the first person I met here and who soon became like family. To Arianna, my lifelong friend, for her companionship and for keeping me motivated every day during the final writing of this thesis. I am especially grateful to Raffaele, whose love, patience, and support have allowed me to realize my ten year long dream of working at the Onsala Observatory. His encouragement and sacrifices have given me the freedom to pursue my goals. To my family who has always been my foundation. Your constant support, encouragement, and belief in me have taught me the importance of following my dreams and persevering through bad times. Every step I take is inspired by your love. To my Master, Li Hongzhi, for protecting and guiding me with his profound teachings of Truthfulness, Compassion, and Tolerance. Un ultimo ringraziamento va a me stessa, per aver superato i miei limiti, le paure e averci creduto con tutto il cuore. Dopo ogni caduta è sempre possibile rialzarsi: non esistono fallimenti, solo nuovi punti di partenza da cui rinascere e sognare ancora più in grande.

Acronyms

CARTA:	Cube Analysis and Rendering Tool for Astronomy
DLR:	German Aerospace Center
DSMC:	Direct Simulation Monte Carlo
ESA:	European Space Agency
FITS:	Flexible Image Transport System
FWHM:	Full Width at Half Maximum
JUICE:	JUpiter ICy moons Explorer
IF:	Intermediate Frequency signal
LIME:	Line Modeling Engine
LO:	Local Oscillator
LTE:	Local Thermal Equilibrium
MPS:	Max Planck Institute for Solar System Research
NASA:	National Aeronautics and Space Administration
SSP:	Sub Solar Point
SWI:	Submillimetre Wave Instrument
VTK:	Visualization Toolkit format

Contents

Part I

Overview

CHAPTER 1

Introduction

In 1610 the Italian astronomer Galileo Galilei observed, for the first time, four small points of light moving in the vicinity of Jupiter. Using a rudimentary telescope of his own fabrication, he studied their motion night after night, realizing that these objects were not stars, but moons in orbit around the giant planet. This discovery posed a significant challenge to the prevailing geocentric model of the universe and supported Copernicus's theory, which, in a revolutionary way, affirmed for the first time that not all celestial bodies rotate around the Earth. In March of that same year, Galileo published his findings in a short treatise titled *Sidereus Nuncius*, a document that would change completely our understanding of the universe and mark the beginning of modern astronomy.

Four centuries later, the Galilean moons, known as Io, Europa, Ganymede, and Callisto, continue to be studied with large interest from astronomers and scientists. Thanks to ground-based observations, spacecraft flybys, and recent data in planetary science, we now know that these moons are complex and unique worlds. In particular, scientific evidence suggests that the three largest Galilean moons, Europa, Ganymede, and Callisto, may harbor subsurface oceans beneath their icy crusts. These findings have placed the Galilean

satellites at the center of astrobiological research. The presence of liquid water, sustained by internal heat sources and possibly interacting with the rocky mantle material, raises the question of whether such peculiar environments could support life.

This chapter reviews the current knowledge of the internal structure and composition of the Icy Galilean moons, with an emphasis on the processes that sustain subsurface liquid water, such as tidal heating and magnetic interactions. Special attention will be given to the possible role of water plumes escaping from their surfaces, and how these phenomena could be linked to the existence of subsurface oceans.

1.1 The Icy Galilean Moons

Europa, Ganymede, and Callisto are often referred to as the Icy Galilean Moons due to their outer icy crusts, primarily composed of water ice.[1]These moons are considered of particular interest among the Solar System's icy bodies, as they present the possibility of subsurface oceans existing beneath their frozen surfaces.

Geophysical models of their internal structure and composition have suggested the presence of these hidden oceans, as discussed in (Van Hoolst et al., 2024; Zimmer et al., 2000). Direct observational evidence supporting this hypothesis was provided by magnetic field measurements from NASA's *Galileo* spacecraft, which orbited Jupiter from 1995 to 2003. These data revealed induced magnetic signatures on Europa, Ganymede, and Callisto, consistent with electrically conductive layers beneath their icy surfaces—most likely subsurface oceans composed of salty liquid water capable of sustaining electrical currents (Kivelson et al., 2000; Khurana et al., 1998). Recent space missions, including *Galileo*, *Juno*, and *Hubble Telescope*, have provided observational data that further support the theory of subsurface oceans and the potential for astrobiological interest on these moons (Kivelson et al., 1996; Roth et al., 2014a; Saur et al., 2015; Connerney et al., 2017).

Ganymede is of particular interest, as it uniquely exhibits not only an induced magnetic field but also a self-sustained intrinsic magnetic field, generated by a convecting, iron-rich liquid core beneath its icy shell (Kivelson et al.,

[1]In contrast, the smallest and innermost Galilean moon, Io, is very geologically active and dry in terms of water content.

1996). This makes Ganymede the only known moon in the Solar System with an internal magnetic dynamo.

Tidal Heating

A key process that could enable the long-term stability of liquid water beneath the icy shells of the Galilean moons is *tidal heating*, a form of internal frictional heating generated by gravitational interactions with Jupiter and its Galilean moons (Chen et al., 2014). This mechanism is driven by the orbital resonance among the Galilean moons, which maintains nonzero orbital eccentricities despite tidal dissipation. All these moons are tidally locked with Jupiter. This means that each moon completes one full rotation around its axis for every orbit around Jupiter, always presenting the same hemisphere towards the planet. Io, Europa, and Ganymede are locked in a *Laplace resonance*, such that for every four orbits completed by Io, Europa completes exactly two, and Ganymede completes one. This phenomenon is referred to as a *4:2:1 mean-motion resonance* (Showman et al., 1997), see Fig. 1.1. In contrast, Callisto is not currently in resonance with the other Galilean moons. However, it may be evolving towards a resonance on a timescale of about 1.5 billion years, as suggested by Lari et al. (2020).

This gravitational configuration creates a stable, repeating orbital pattern in which the moons regularly exert gravitational tugs on each other. These interactions prevent their orbits from becoming perfectly circular, maintaining a small but significant orbital eccentricity. Because the moons' orbits are slightly elliptical, the gravitational force from Jupiter varies throughout their orbit. This leads to periodic stretching and compression of each moon, especially in their interior layers. This repeated deformation causes internal friction within the ice and rocky mantles–a process known as *viscoelastic dissipation*–which converts mechanical energy into thermal energy (Moore et al., 2003).

In the case of Europa, this heating is concentrated beneath the ice shell and provides sufficient energy to sustain a global subsurface ocean. For Ganymede, which is larger and more massive and farther from Jupiter, tidal heating is weaker but still significant, especially when combined with radiogenic heating, generated by the decay of radioactive isotopes found in the moon's interior. Io, the innermost and most volcanically active of the Galilean moons, experiences the most extreme tidal heating and is the most volcanically active body in

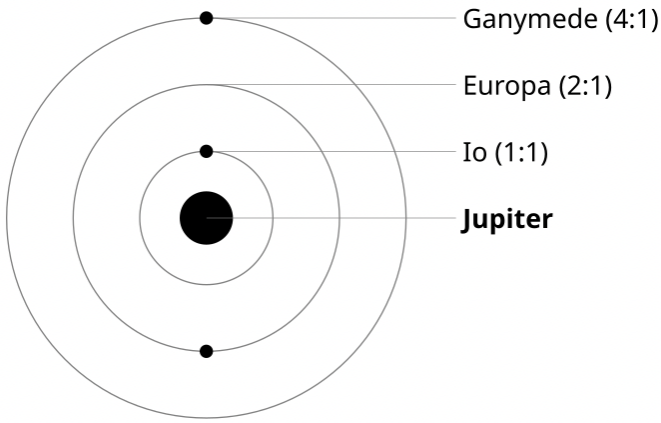

Figure 1.1: Schematic representation of the Laplace resonance among Jupiter's moons Io, Europa, and Ganymede. For every 4 orbits of Io, Europa completes 2 and Ganymede 1, maintaining a 4:2:1 orbital ratio. **Credit**:Wikipedia Commons

the Solar System. In contrast, Callisto, being the farthest of the Galilean moons from Jupiter, experiences tidal forces that are less than 10% of those at Europa's distance. As a result, tidal heating on Callisto is negligible.

It is hypothesised that tidal heating may be capable of supplying a sufficient quantity of energy to ensure the presence of liquid water beneath the icy crusts of the icy Galilean moons over geological timescales (Ojakangas et al., 1989). Another factor that determines if a subsurface ocean can be kept liquid over geological time scales is its composition. Water mixed with other compounds, such as ammonia or salts, can exhibit lower melting points enabling the the preservation of liquid water even at temperatures below zero (Meier et al., 1992). An example of this is Saturn's moon Enceladus, where the tidal heating mechanism is not sufficient for generating heat, given the thickness of its icy crust, which is 30 km (Spencer et al., 2006). Consequently, an additional agent is required to facilitate the process of heat generation. The mass spectrometer on the Cassini mission has revealed that the water on Enceladus is not a pure substance, but rather a mixture composed of carbon dioxide, carbon monoxide, formaldehyde, ammonia, and methane (Postberg et al., 2009). These compounds have been demonstrated to function as an-

tifreeze agents, allowing for the existence of liquid water under the thick ice crust.

Internal Structure and Composition

Data from the *Galileo* magnetometer suggest that Europa and Ganymede possess a layered internal structure, consisting of a metallic core, a silicate mantle, and overlying water-rich layers, either in liquid or ice form. As shown in Fig. 1.2, Ganymede is believed to have a complex internal structure, with an ice shell estimated to range from 50 to 150 km in thickness, a subsurface ocean that could extend over 100 km deep, and a lower layer of warm, ductile high-pressure ice situated above the rocky mantle (Kivelson et al., 2002a; Van Hoolst et al., 2024). These conclusions are based on geophysical models and magnetic field measurements from the *Galileo* spacecraft, which revealed both an induced magnetic field consistent with a salty, conductive liquid layer beneath the ice, and an intrinsic magnetic field generated by a convecting, iron-rich liquid core (Kivelson et al., 1996; Kivelson et al., 2002b). This unique combination of intrinsic and induced magnetic fields provides some of the strongest direct evidence for Ganymede's fully differentiated interior.

Europa has a simpler structure, consisting of a metallic core, a silicate mantle, and a relatively thin ice shell – estimated to be 10–30 km thick – beneath which lies a subsurface ocean (Pappalardo et al., 1999; Kivelson et al., 2000) (see Fig. 1.2). The proximity of the ocean to the silicate rocky mantle allows for potential water-rock interactions and hydrothermal activity which could enhance Europa's habitability by facilitating chemical exchange and energy availability (Pappalardo et al., 1999).

Callisto, in contrast, exhibits a less differentiated internal structure compared to Ganymede and Europa. Its icy crust is estimated to be between 80 and 150 km thick, beneath which lies a possible subsurface ocean approximately 150–200 km deep, as suggested by magnetic field measurements from the *Galileo* mission (Khurana et al., 1998; Anderson et al., 2001; Vance et al., 2018). Below this ocean, as depicted in Fig. 1.2, models suggest the presence of a high-pressure ice layer, followed by a mantle composed of a partially mixed ice-rock composition. At greater depths, the existence of a small rocky core remains uncertain (Vance et al., 2018; Bennacer et al., 2025). Unlike Europa and Ganymede, Callisto lacks significant tidal heating because it is not part of the orbital resonance that drives internal friction and heating in the other

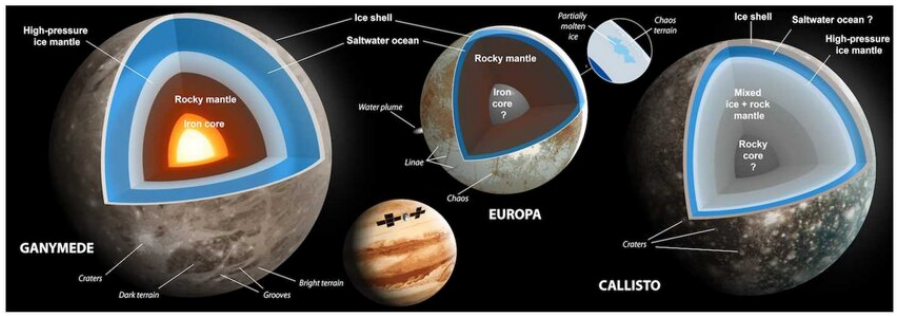

Figure 1.2: Schematic representation of the interior structures of Ganymede, Europa, and Callisto based on *Galileo* data. The diagram highlights the significant structural differences among the moons, including Ganymede's differentiated structure with a thick hydrosphere and iron-rich core. The internal composition of Europa and Callisto is less certain, particularly regarding the presence of an iron core in Europa and the degree of ice-rock separation in Callisto. The thickness, depth and composition of the saltwater subsurface oceans are still poorly constrained. Galileo data are not fully conclusive about the existence of an ocean in Callisto. **Credit**:Van Hoolst et al. (2024).

moons. This reduced tidal dissipation results in a lower internal heat budget, which likely limits geological activity and has prevented full differentiation of its interior (Bennacer et al., 2025).

Water Plumes

One of the most revealing indicators of subsurface oceanic activity on icy moons would be the presence of localised water vapor plumes – jets of gas and ice particles that escape into space through fissures in the outer ice shell. These outgassing events offer a unique opportunity to access a proxy to the chemical composition of the interior without the need for direct subsurface sampling.

These peculiar phenomena have been specifically observed on Enceladus, one of the major moons of Saturn. In 2005, the *Cassini* spacecraft detected water plumes erupting from the so-called "tiger stripes" near the south pole

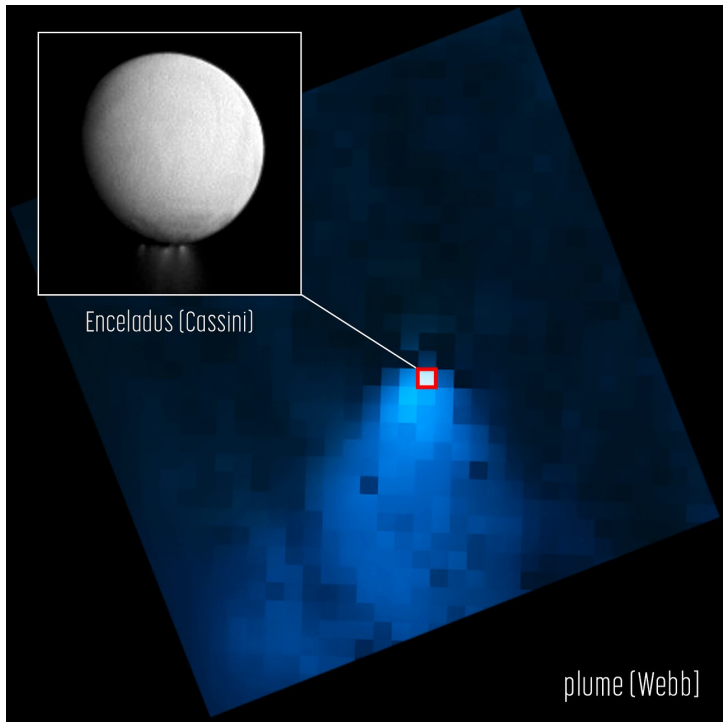

Figure 1.3: A water vapor plume emanating from the south polar region of Enceladus, as observed through a combination of Cassini spacecraft data and recent observations from the James Webb Space Telescope (JWST). The plume extends over more than 9600 kilometres — long enough to stretch across the Eurasian continent from Ireland to Japan, far beyond previous estimates based solely on Cassini data. **Credit:** NASA/JPL-Caltech/ESA/STScI.

(C. J. Hansen et al., 2006; Waite et al., 2006) (see Figure 1.3). Spectral and compositional analyses revealed that the plumes are made of water vapor, salts, molecular hydrogen, and simple organics, indicating the existence of a subsurface ocean interacting with a silicate core – possibly through hydrothermal processes (Postberg et al., 2009; Hsu et al., 2015).

Similar activity may also occur on Europa and Ganymede. Observations from the Hubble Space Telescope in 2012 and 2016 identified localized ultraviolet emissions consistent with water vapor plumes originating from near the moon's equator and south pole (Roth et al., 2014b; Sparks et al., 2016). Although the detections remain episodic and difficult to confirm, they suggest that Europa's ice shell may occasionally vent material from the subsurface ocean – especially in regions subject to tidal stress – and have prompted a series of follow-up studies (Sparks et al., 2016; Jia et al., 2018; Paganini et al., 2019) aimed at confirming plume activity through independent methods.

While no plumes have been directly detected on Ganymede, modeling studies – supported by auroral asymmetries observed by Hubble – suggest that localized releases of water vapor may occur under specific thermodynamic and orbital conditions (Saur et al., 2015; Saur et al., 2022). These transient expulsions could be driven by cryovolcanic eruptions[2] or by the slow seepage of subsurface volatiles through fractures in the crust.

The identification, localisation and study of water plumes is thus central to evaluating the habitability of icy moons and identifying promising targets for future exploration.

1.2 Vostok Lake: A Terrestrial Analog for Icy Moon Oceans

In the study of potential subsurface oceans on icy moons such as Europa, Ganymede, and Callisto, scientists face the question of how life could thrive in such extreme environments. The question that arises is how organisms could survive beneath vast layers of ice, in conditions of high pressure and subzero temperatures, with minimal to no sunlight. To understand the potential habitability of subsurface oceans on icy moons, we can look to an extreme

[2]Cryovolcanism refers to "cold volcanism," where water, ammonia, methane, or other volatiles erupt from the subsurface instead of molten rock, as observed for instance on Enceladus and Triton.

environment here on Earth: Lake Vostok in Antarctica. Discovered in the 1960s by Soviet researchers through satellite imagery and ice-penetrating pulse radar, Lake Vostok lies buried beneath approximately 4 kilometers of ice, making it one of the largest subglacial lakes known.

The thick ice sheet acts as a natural barrier, isolating the lake from surface influences and preserving a unique ecosystem. The lake has been isolated from the surface for about 15 to 25 million years, and it remains liquid due to the pressure exerted by the overlying ice and the geothermal heat from the Earth's interior. The temperature of the water at the bottom of the Lake Vostok is around $-3°C$, which is below the normal freezing point but remains liquid due to the combined effects of high pressure (approximately 350–400 atmospheres) and the presence of dissolved substances such as salts or gases (Priscu et al., 2003; Siegert et al., 2001). A similar situation is expected in the subsurface oceans of icy moons like Europa and Ganymede, where high overburden pressure – potentially reaching thousands of atmospheres – combined with antifreeze agents (e.g., magnesium sulfate or ammonia) could maintain liquid water at sub-zero temperatures.

Despite the extreme conditions, scientists have identified a variety of microbial life forms, including bacteria and archaea. These organisms appear to be specially adapted to survive in the cold, dark, and oxygen-poor environment and can survive in the lake by using chemical energy from the rocks beneath the ice, rather than relying on sunlight. These microbes likely utilize a process called "chemosynthesis," where they convert chemical compounds such as methane, hydrogen, and sulfur into energy, much like life around Earth's hydrothermal vents. In fact, the microbes found in Lake Vostok are hypothesized to be similar to those found in other extreme environments, such as deep-sea hydrothermal vents and acidic hot springs (Ridley et al., 2014; Christner et al., 2006).

Studying Lake Vostok can provide important information into how life might endure in similar extreme conditions on icy moons. The isolation and extreme physical parameters mirror, to some extent, the environment expected beneath the thick ice shells of Europa, Ganymede, and other icy worlds. Therefore, Lake Vostok can be seen as a natural laboratory for investigating whether and how life can arise in extraterrestrial subsurface oceans and this can help to guide future exploration and mission planning.

CHAPTER 2

Ganymede

Ganymede is the largest of the Galilean moons and the most massive natural satellite in the Solar System. With a diameter of approximately 5268 km, it is larger than the planet Mercury, although it has only about half of Mercury's mass (Anderson et al., 1996; Schubert et al., 2004). Its average density of about 1.94 g/cm³ suggests a mixture of silicate rock and water ice, which is consistent with the idea of a fully differentiated interior, as discussed in Chapter 1.1. Ganymede's orbital period around Jupiter is approximately 7.15 Earth days. Like the other Galilean moons, it is tidally locked, always presenting the same hemisphere toward the planet.

As the only known satellite in our solar system to possess an intrinsic magnetic field (e.g., Gurnett et al. (1996); Kivelson et al. (2002b)), Ganymede forms a small magnetosphere within the much larger magnetosphere of Jupiter. Jupiter's magnetosphere rotates in about 10 hours — much faster than Ganymede's orbital period. As a result, the moon moves through a stream of magnetospheric plasma flowing past it at high relative velocities. This interaction between the two magnetic fields strongly influences the morphology of Ganymede's atmosphere and shapes its auroral emissions (Hall et al., 1998; Feldman et al., 2000; McGrath et al., 2007; Saur et al., 2015; Kleer

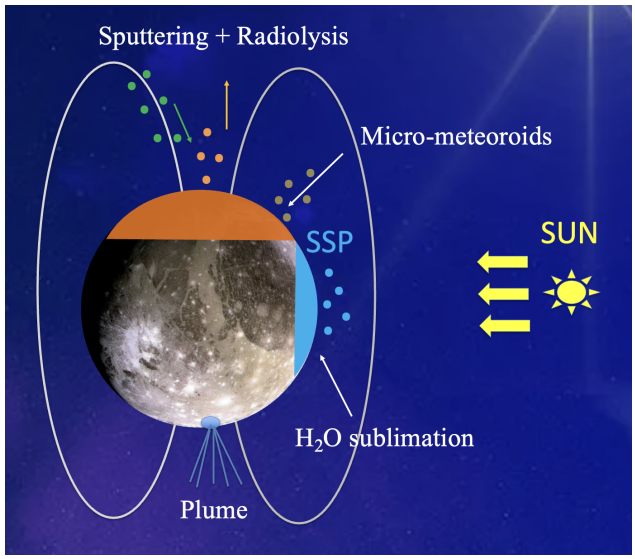

Figure 2.1: A schematic view of the processes occurring in the atmosphere of Ganymede. **Credit**:Margheri.

et al., 2023).

In the following sections, we focus on the composition of Ganymede's atmosphere, with particular attention to the physical processes that contribute to the distribution of water vapor, and introduce the theoretical models used to investigate its complexity.

2.1 Atmosphere composition and processes

Ganymede is believed to have a thin and tenuous atmosphere primarily composed of water and other oxygen and hydrogen-based neutral species. The atmospheric composition should, to some extent, reflect the chemical composition of its surface, which is predominantly water ice (Ligier et al., 2019; Bockelée-Morvan et al., 2024), as also observed on Europa (Pilcher et al., 1972; Showman et al., 1999; G. B. Hansen et al., 2004).

Ganymede's atmosphere was first investigated in detail during the *Galileo* spacecraft's close flyby in 1997. During this mission, atomic hydrogen was

detected through Lyman-alpha emission in the ultraviolet spectrum with an estimated column density of approximately $9 \times 10^{12}\,\mathrm{cm}^{-2}$ (Barth et al., 1997). Subsequent observations by the *Hubble Space Telescope* in 1998 revealed the presence of both atomic and molecular oxygen (Hall et al., 1998). The oxygen species were predominantly found in the polar regions or at latitudes above 45° (Feldman et al., 2000). This distribution can be explained by Ganymede's intrinsic magnetic field, which behaves like a dipole. The magnetic field lines are closed within ±45° latitude but open at higher latitudes.

At the Subsolar Point (SSP) – the region where solar radiation strikes the surface perpendicularly – surface temperatures reach 80-150 K (Marconi, 2007; Plainaki et al., 2015; Roth et al., 2021). This range reflects local variations due to differences in surface composition, albedo, and topography, and solar incidence (Spencer, 1987; Orton et al., 1996; Roth et al., 2021). In this region, water ice sublimates efficiently, injecting water molecules into the atmosphere and locally increasing their density (Fig. 2.1). Sublimation at the SSP is considered the dominant source of water in Ganymede's exosphere (Marconi, 2007).

In the polar regions, where Ganymede's magnetic field lines are open, energetic ions from Jupiter's magnetosphere travel along the field lines and impact the icy surface. This impact releases a variety of molecules through two distinct processes:

- *Sputtering:* Energetic heavy ions (e.g., O^+, S^+, O^{++}, S^{+++}) hit the surface ice, physically ejecting molecules such as H_2O, OH, O_2, and H_2, and atomic oxygen and hydrogen.

- *Radiolysis:* High-energy particles break water molecules into H_2 and O_2. While hydrogen tends to escape into space due to its low mass (Trumbo et al., 2023), oxygen remains gravitationally bound and gradually accumulates in the exosphere (Tinner et al., 2024).

Both processes are most efficient at latitudes above 45°, although the most energetic Jovian plasma ions (e.g., O^{++}, S^{+++}) can also penetrate the magnetic field near the equator on the trailing hemisphere, causing additional sputtering there (Poppe et al., 2018). Micro-meteoroids impacts also contribute to enrich Ganymede's exosphere by sputtering surface ice and releasing water and oxygen species (Tosi et al., 2024). Although this contribution

is generally smaller than that from sublimation or polar irradiation, it acts globally across the surface.

Fig.2.1 summarizes the combined effects of sublimation at the SSP, polar sputtering and radiolysis, and micrometeoroid impacts. These processes produce a highly structured and dynamic exosphere, with species distributions varying with latitude, local time, and the position of the SSP, leading to complex spatial and temporal variability.

2.2 Theoretical models of water distribution in Ganymede's atmosphere

Understanding the complex atmosphere of Ganymede requires to combine in situ observations and theoretical modeling. While direct measurements are limited, theoretical models have been developed to simulate the spatial distribution of neutral species in Ganymede's exosphere and in particular water. Earliest modeling efforts of Ganymede's atmosphere date back to the 1970's, when Yung and McElroy (1977) published a hydrostatic, spherically symmetric, isothermal diffusive model of Ganymede's O_2 atmosphere. Since then, models have become significantly more complex, incorporating information now available both from observations and from laboratory measurements.

Recent models include the one published by Marconi (2007), a 2D axisymmetric kinetic model that uses surface sputtering and water sublimation as atmospheric source processes. In the model, sputtering by energetic particles produces H_2O, OH, O_2, O, H, and H_2, while sublimation releases only H_2O. The model assumes that Ganymede's exosphere is symmetric around the axis connecting the Sun and Ganymede. This means that variations are calculated only as a function of latitude (from the subsolar point toward the poles) and altitude, while differences in longitude at the same latitude are neglected. This assumption of axisymmetry is justified because the main source of water vapor—sublimation—depends primarily on solar illumination, which varies mainly with latitude, and sputtering occurs predominantly along open magnetic field lines near the poles. Therefore, the largest variations in density and composition occur with latitude and altitude, while longitudinal differences are comparatively small. Under this assumption, the modeled H_2O column density decreases approximately following a cosine law away from the subsolar point, and then drops sharply beyond about 45° latitude (Fig. 2.2). This

simplification, reasonable given the limited observational constraints, enables a full kinetic treatment of the composition, structure, dynamics, and escape of both sublimated and sputtered species. The results indicate that, outside a narrow region near the subsolar point, the exosphere is predominantly collisionless.

Figure 2.2, taken from Marconi (2007), presents the resulting radial column density of the main neutral species (integrated along a radial coordinate through Ganymede's center) as a function of the angle from the Subsolar Point. The model reveals a two-part atmosphere: the *sublimation region*, extending from the subsolar point (latitude = 0°) to roughly the inner boundary of the open field line region ($\sim 45°$), and the *sputtering region*, which extends from $\sim 45°$ to the antisubsolar point (180°). In the sublimation region, the column density is dominated by water vapor released from the sublimation of surface ice, peaking near the subsolar point at $\sim 6 \times 10^{15}\,\mathrm{cm}^{-2}$. Other species in this region originate from photochemical processes or are transported from the sputtering region. Beyond $\sim 45°$ latitude, the abundance of H_2O drops sharply due to lower surface temperatures, consistent with the reduced efficiency of both sublimation and sputtering. In these colder regions, other species become relatively more abundant, but a detailed discussion lies beyond the scope of this section, which focuses on water vapor. Fig. 2.2 also demonstrates the 2D nature of this model, with its symmetry axis through the SSP, making it possible to define the sublimation and sputtering regions using ranges in latitude.

While Marconi's 2D model provided the first detailed spatial distributions of H_2O and O_2, subsequent studies have extended these results using fully three-dimensional approaches. Turc et al. (2014) applied a 3D collisionless test-particle model, confirming Marconi's results regarding H_2O and O_2 distributions, and further studied atmospheric response to time-varying conditions such as passage into Jupiter's shadow and intrinsic plasma variations. Plainaki et al. (2015) incorporated spatially varying energetic ion precipitation (H^+, O^+, S^+), showing that sputtered H_2O closely follows the ion distribution with enhanced densities in the trailing hemisphere. Leblanc et al. (2017) applied a 3D parallelized collisional model, refining the spatial and temporal variability of H_2O and O_2 and revealing hemispheric asymmetries due to ion precipitation and seasonal effects. More recently, Plainaki et al. (2020) and Vorburger et al. (2022) used modern 3D Monte Carlo simulations to investi-

gate localised H_2O sources, surface temperature effects, and plasma-surface interactions, highlighting significant longitudinal and hemispheric variability in water production.

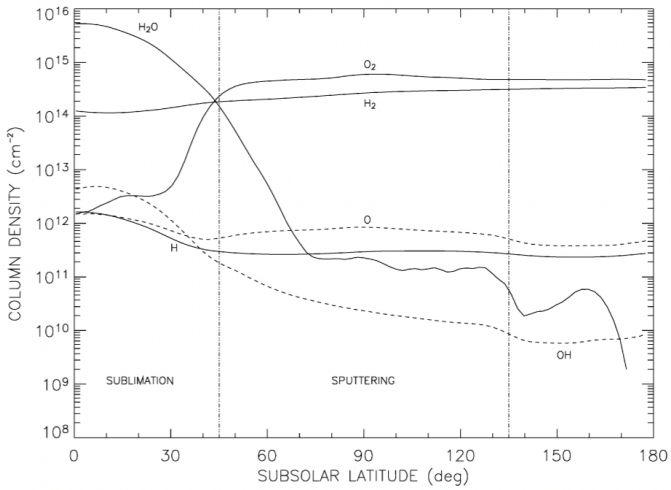

Figure 2.2: Radial column densities of various neutral species as a function of angular distance from the subsolar point, based on the 2D kinetic model by Marconi (2007). The H_2O profile decreases roughly following a cosine law away from the subsolar point and drops sharply beyond 45° latitude, illustrating the 2D nature of the model. **Credit**:Marconi (2007).

This thesis adopts the atmospheric water emission model developed by Wirström et al. (2020), which uses analytical simplifications of the theoretical results by Marconi (2007) for the water properties of Ganymede's atmosphere. The model by Wirström et al. (2020) assumes analytical vertical distributions of water number density and temperature extending from the surface up to about 450 km altitude, with variations depending on the angular distance from the subsolar point, based on the model by Marconi (2007). A detailed description and application of this model is presented in Chapter 6, where these profiles are used as input to represent the physical conditions in the exosphere of Ganymede.

CHAPTER 3

Exploring Ganymede with SWI/JUICE

Theoretical models of Ganymede's exosphere are especially valuable for planning observation strategies and interpreting data for upcoming space missions. This chapter gives an overview of the ongoing JUICE mission and highlights the role of one of its onboard instruments, the Submillimeter Wave Instrument (SWI), which will be useful for observing Ganymede's exosphere and detecting potential water plumes.

3.1 The JUICE Mission

To investigate the Galilean moons in greater detail, the European Space Agency (ESA) developed the JUpiter ICy moons Explorer, also known as JUICE mission. The mission was selected in 2012 as the first Large-class mission of ESA's Cosmic Vision program (2015–2025) (ESA, 2012). JUICE was successfully launched on April 14$^{\text{th}}$, 2023, aboard an Ariane 5 rocket from the Guiana Space Center in French Guiana (ESA, 2023a). The spacecraft is currently on a complex interplanetary trajectory and is expected to arrive at the Jovian system in July 2031, after performing a series of gravity-assist maneuvers involving Earth and Venus (ESA, 2023c). This long cruise

phase will allow the spacecraft to gradually gain the velocity needed to reach Jupiter's orbit while minimizing fuel consumption. Once it arrives, JUICE will spend at least three and a half years studying Jupiter and its three icy moons: Ganymede, Europa and Callisto. The mission's primary objective is to understand whether these peculiar environments could support life, focusing on key indicators of habitability such as the presence of liquid water, energy sources, and essential chemical ingredients. During the final phase of the mission, JUICE will enter into orbit around Ganymede and this will be the first time a spacecraft will orbit around a moon other than our own, providing an unprecedented opportunity to study Ganymede's surface, interior, exosphere, and magnetosphere in great detail.

To accomplish its goals, JUICE is equipped with a suite of ten scientific instruments (ESA, 2023d; ESA, 2023b), developed by international collaborations across Europe, the United States, and Japan. These include cameras, spectrometers, radar, magnetometers, submillimeter and radio instruments as illustrated in Fig. 3.1. Together, these instruments will make it possible to:

- Characterize the surface composition and geology of the icy moons;
- Detect and analyze thin atmospheres and exospheres, including potential water plumes;
- Measure the internal structures and potential subsurface oceans using radar sounding and gravimetry;
- Study the Jovian magnetosphere and its interaction with the moons;
- Observe the dynamics of Jupiter's atmosphere, auroras, and radiation environment.

Among the scientific payloads on board JUICE, the *Submillimeter Wave Instrument* (SWI) is designed to investigate the temperature structure, composition and dynamics of Jupiter's atmosphere and characterise the exospheres of its icy moons. Working in the submillimeter range, SWI is particularly suitable for detecting and analysing rotational spectral lines of water vapor and other molecular species present in the atmospheres.

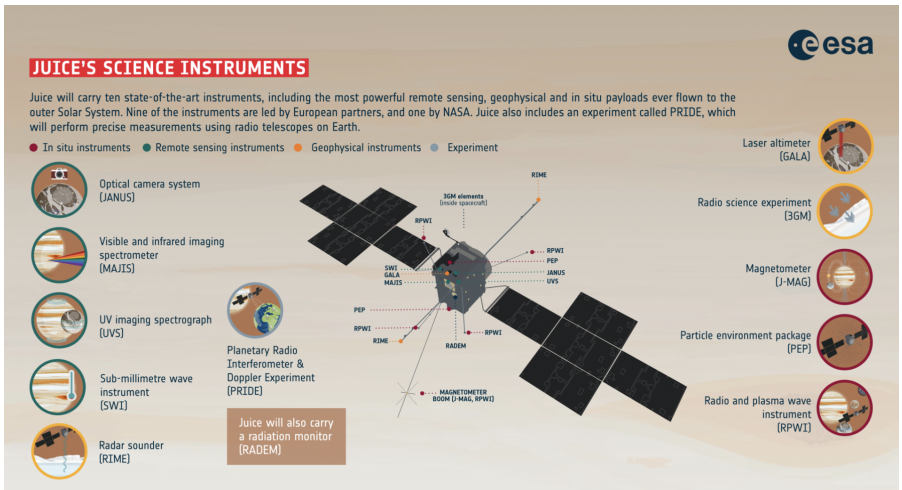

Figure 3.1: The ten scientific instruments aboard the JUICE spacecraft. **Credit**:ESA

3.2 The Submillimeter Wave Instrument (SWI)

The *Submillimeter Wave Instrument* (SWI) was developed by the German Aerospace Center (DLR), led from Max Planck Institute for Solar System Research (MPS) with major hardware and science contributions from France, Sweden, Switzerland, and Japan (ESA, 2023e).

SWI features an offset Cassegrain antenna with a 29 cm moveable main reflector (M1) and a fixed secondary reflector (M2), see Fig. 3.2). The main reflector is capable of moving its pointing within ±72° along-track and ±4° cross-track with reference to the nominal orientation of the JUICE spacecraft in flight, allowing it to perform a wide range of observation geometries. A view of SWI mounted on the JUICE spacecraft prior to launch is shown in Fig. 3.3, highlighting its compact integration within the payload.

SWI is a high-resolution instrument composed of two independent heterodyne receivers, each covering a distinct frequency band: Band 1 covers 530–625 GHz (wavelengths 479–565 μm), while Band 2 covers 1080–1275 GHz (wavelengths 235–278 μm). Each receiver uses the heterodyne detection technique, mixing the incoming high-frequency signal with a stable signal gener-

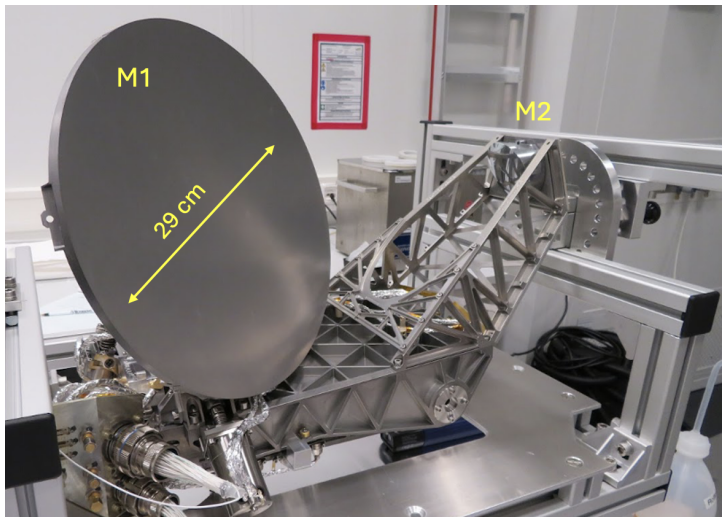

Figure 3.2: The SWI instrument in the lab at MPS before delivery to ESA. The image shows SWI steerable parabolic 29 cm antenna, the main (M1) and secondary (M2) reflectors. **Credit**: MPS.

Figure 3.3: JUICE being unpacked after delivery to French Guyana for the launch. SWI can be seen mounted to the left, marked by a circle for extra clarity. **Credit**: ESA-CNES-Arianespace

ated by a local oscillator (LO) and producing an intermediate frequency signal (IF) that preserves the spectral information of the original signal but at a lower frequency making it easier to amplify and analyse with high precision. .SWI is equipped with four spectrometers that analyse the IF signal coming from the receivers: two high-resolution spectrometers, CTS1 and CTS2, each with 10^4 channels over 1 GHz, and two lower-resolution spectrometers, ACS1 and ACS2, each with 10^3 channels over 4 GHz. The high-resolution spectrometers provide a spectral resolving power of up to $\nu/\Delta\nu \approx 10^7$, enabling extremely fine spectral resolution, the detection of weak signals, and highly accurate Doppler shift measurements, essential for studying atmospheric composition and dynamics.

SWI operates in the harsh environment of deep space, where extreme conditions such as intense radiation, temperature fluctuations, and strict limitations on size and weight prevail. To address these challenges, its electronic components are miniaturised – that is, made very compact to save space and reduce weight – and radiation-hardened, which means they are specifically built to resist damage caused by space radiation. Additionally, the components are thermally stable, ensuring consistent performance despite temperature fluctuations.

SWI is designed to investigate the atmospheres and surface interactions of the icy Galilean moons, with particular emphasis on Ganymede and Europa. Its primary objectives in this context include:

- Characterise the distribution, variability, and composition of the tenuous atmospheres and exospheres of Ganymede and other icy moons.
- Detect and analyse water vapor, including potential plume activity, by targeting specific rotational spectral lines.
- Derive wind velocities and temperature profiles through Doppler shift analysis of narrow molecular emission lines.
- Investigate surface properties and their contribution to atmospheric production via processes such as sublimation and sputtering.

In addition to these goals, SWI also pursues broader scientific objectives within the Jovian system, including:

- Investigate the composition and wind structure of Jupiter's stratosphere through high-resolution spectral observations.

- Measure isotopic ratios of key molecular species to gain insights into the formation and evolutionary processes of Jupiter-like planets.

Table 3.1 lists the main spectral lines observable by SWI, with a focus on water vapor lines critical for studying icy moon atmospheres. Since the two receivers can be tuned independently and operated simultaneously, any combination of lines from Band 1 and Band 2, respectively, can be targeted in the same observation.

Molecule	Transition frequency (GHz)	Transition
Band 1		
o$-H_2^{16}O$	556.936 GHz	$1_{10} - 1_{01}$
o$-H_2^{16}O$	620.701 GHz	$5_{32} - 4_{41}$
o$-H_2^{18}O$	547.676 GHz	$1_{10} - 1_{01}$
o$-H_2^{17}O$	552.021 GHz	$1_{10} - 1_{01}$
HDO	599.927 GHz	$2_{11} - 2_{02}$
Band 2		
p$-H_2^{16}O$	1113.343 GHz	$1_{11} - 0_{00}$
p$-H_2^{16}O$	1228.789 GHz	$2_{20} - 2_{11}$
p$-H_2^{16}O$	1207.639 GHz	$4_{22} - 4_{13}$
o$-H_2^{16}O$	1153.127 GHz	$3_{12} - 2_{21}$
o$-H_2^{16}O$	1097.365 GHz	$3_{12} - 3_{03}$
o$-H_2^{16}O$	1162.912 GHz	$3_{21} - 3_{12}$
o$-H_2^{18}O$	1181.394 GHz	$3_{12} - 2_{21}$
o$-H_2^{18}O$	1095.627 GHz	$3_{12} - 3_{03}$
o$-H_2^{18}O$	1136.703 GHz	$3_{21} - 3_{12}$
o$-H_2^{17}O$	1168.130 GHz	$3_{12} - 2_{21}$
o$-H_2^{17}O$	1096.410 GHz	$3_{12} - 3_{03}$
o$-H_2^{17}O$	1148.970 GHz	$3_{21} - 3_{12}$
HDO	1267.043 GHz	$3_{13} - 2_{12}$
HDO	1217.258 GHz	$3_{21} - 3_{12}$
HDO	1164.770 GHz	$4_{22} - 4_{13}$

Table 3.1: Representative water spectral lines observable in the exospheres of the icy moons. The SWI instrument can be tuned to target any of these transitions.

To achieve the scientific objectives outlined above, SWI will operate in different observation modes depending on the distance of JUICE from the

target (Cavalié et al., 2021):

- **Single Point Stare:** when the instrument continuously observes a fixed and specific point on the target. It is typically employed when the moon or the planet is unresolved within the beam (e.g., at large distances) or when long time-series measurements are required.

- **2D Mapping:** A series of observations covering a two-dimensional region of the moon's or planet's surface, used when the target is close enough to be partially or fully resolved. This mode allows to create spatial maps of molecules, enabling the detection of localised sources such as water plumes in the tenuous atmospheres of icy moons. An example of this observation mode for Ganymede is shown in Figure 3.4.

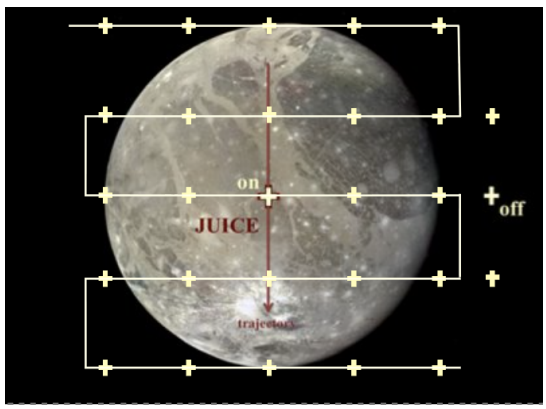

Figure 3.4: Example of the 2D mapping observation mode for Ganymede. Credit: T. Cavalié and JUICE/SWI science team.

- **Limb Scan:** Observations across the limb of the moon or the planet, allowing more detailed characterisation of the atmosphere. This geometry enhances the sensitivity to optically thin emissions and is particularly suited to derive vertical density and temperature profiles, complementing nadir or mapping observations. Using long integrations close to the limb, where density is expected to be highest, will also be the primary observing mode for detecting less abundant molecules and isotopologues.

As mentioned above, the choice of observation mode depends on the spacecraft distance to the target and the corresponding angular size in the instrument beam and the specific scientific goals of each observation campaign. For example, after entering into orbit around Jupiter, SWI will observe one or several of the Galilean moons for one hour per day in what is called the moon monitoring campaign. This will enable the characterisation of the evolution of their atmospheres as well as identification of transient features.

The high-resolution spectral data provided by SWI can be interpreted using appropriate modeling techniques, which allow the study of atmospheric parameters such as temperature, density, and velocity fields, thus providing a deeper understanding of Ganymede's exosphere — the main focus of this thesis.

CHAPTER 4

Radiative Transfer Theory

This chapter provides a concise overview of radiative transfer and spectral line theory. The discussion includes the two-level system as a fundamental example, the case of local thermodynamic equilibrium (LTE), and departures from LTE. Finally, particular attention is given to rotational transitions of water molecules, which are essential for the studies of icy moons atmospheres, which is the focus of this thesis. The chapter follows the general formalism used in Rohlfs et al. (2004).

4.1 The Radiative Transfer equation

The radiative transfer equation describes how the intensity of electromagnetic radiation changes as it travels through a medium. For example, this occurs when radiation passes through the atmosphere of a planet or moon. Consider a thin slab of a homogeneous medium with an infinitesimal thickness ds. The specific intensity of radiation at frequency ν, denoted I_ν, describes the amount of radiant energy traveling per unit area A, per unit time t, per unit frequency ν, and per unit solid angle Ω in a given direction:

$$I_\nu = \frac{dE}{dA\, dt\, d\nu\, d\Omega}, \tag{4.1}$$

where I_ν is expressed in units of $\mathrm{erg\,s^{-1}\,cm^{-2}\,Hz^{-1}\,sr^{-1}}$. As the radiation passes through the slab can be affected by both absorption and emission by the medium, as illustrated in Figure 4.1. Let ϵ_ν be the *emission coefficient*

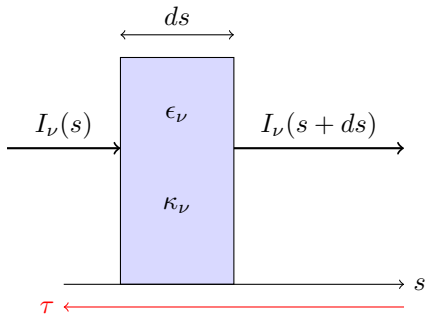

Figure 4.1: Illustration of radiative transfer in an infinitesimally thin slab of a homogeneous medium. The incoming intensity $I_\nu(s)$ enters the slab of thickness ds, where it is absorbed and emitted with coefficients κ_ν and ϵ_ν, resulting in outgoing intensity $I_\nu(s+ds)$. The optical depth τ increases toward the source (red arrow), opposite to the direction of s.

[erg $\mathrm{s^{-1}}$ $\mathrm{cm^{-3}}$ $\mathrm{Hz^{-1}}$ $\mathrm{sr^{-1}}$] and κ_ν the *absorption coefficient* [$\mathrm{cm^{-1}}$]; then the intensity of the radiation exiting the layer, $I_\nu(s+ds)$, is related to the incoming intensity $I_\nu(s)$ by the relation:

$$I_\nu(s+ds) = I_\nu(s) - \kappa_\nu I_\nu(s)ds + \epsilon_\nu ds. \tag{4.2}$$

The term $-\kappa_\nu I_\nu(s)$ describes the attenuation of the radiation due to absorption, while $\epsilon_\nu\, ds$ accounts for the increase in intensity due to local emission. Defining the infinitesimal change in intensity as:

$$dI_\nu = I_\nu(s+ds) - I_\nu(s),$$

and taking as limit $ds \to 0$, we obtain the differential form of the radiative transfer equation:

$$\frac{dI_\nu}{ds} = -\kappa_\nu I_\nu(s) + \epsilon_\nu. \tag{4.3}$$

It is often convenient to rewrite the radiative transfer equation in terms of a quantity known as the *source function*, defined as the ratio of the emission coefficient to the absorption coefficient:

$$S_\nu = \frac{\epsilon_\nu}{\kappa_\nu}. \tag{4.4}$$

This reformulation is useful because the source function S_ν has the same dimensions as the specific intensity and, instead of treating the emission and absorption coefficients separately, it combines both processes into a single quantity. This effectively describes the state of the local radiation field as it interacts with the medium. Substituting S_ν into Eq. 4.3, gives:

$$\frac{dI_\nu}{ds} = -\kappa_\nu \left[I_\nu(s) - S_\nu\right]. \tag{4.5}$$

In this form, the equation clearly shows that the change in intensity along the path is determined by the difference between the specific intensity I_ν and the source function S_ν. When $I_\nu > S_\nu$, absorption dominates and the intensity decreases. Conversely, when $I_\nu < S_\nu$, emission dominates and the intensity increases. If $I_\nu = S_\nu$, the medium and the radiation field are in radiative equilibrium, and the intensity remains constant.

To measure how much material the radiation passes through, it is useful to introduce the concept of *optical depth*, τ_ν, defined as

$$d\tau_\nu = -\kappa_\nu \, ds, \tag{4.6}$$

By convention, the optical depth is defined to be zero at the observer's position and increases toward the source of radiation, see Figure 4.1. This allows us to rewrite the radiative transfer equation in terms of τ_ν, simplifying the description of absorption and emission along the path:

$$\frac{dI_\nu}{d\tau_\nu} = I_\nu - S_\nu, \tag{4.7}$$

The solution to this differential equation describes how the radiation inten-

sity emerging from a medium depends on properties and the amount of that material. Equation 4.7 can be solved formally by multiplying both sides by $e^{-\tau_\nu}$:

$$\int_0^{\tau_\nu(s)} e^{-\tau_\nu} \frac{dI_\nu}{d\tau_\nu}\, d\tau_\nu = \int_0^{\tau_\nu(s)} (I_\nu - S_\nu)\, e^{-\tau_\nu}\, d\tau_\nu. \tag{4.8}$$

Integrating by parts:

$$\left[I_\nu e^{-\tau_\nu}\right]_0^{\tau_\nu(s)} + \int_0^{\tau_\nu(s)} I_\nu\, e^{-\tau_\nu}\, d\tau_\nu = \int_0^{\tau_\nu(s)} (I_\nu - S_\nu)\, e^{-\tau_\nu}\, d\tau_\nu. \tag{4.9}$$

Since τ_ν is now the variable of integration, we also introduce a variable τ'_ν inside the integral to distinguish it from the upper limit $\tau_\nu(s)$, obtaining:

$$I_\nu\big(\tau_\nu(s)\big)\, e^{-\tau_\nu(s)} - I_\nu(0) = -\int_0^{\tau_\nu(s)} S_\nu\, e^{-\tau'_\nu}\, d\tau'_\nu, \tag{4.10}$$

and expressing the intensity measured at the observer where $\tau = 0$, as a function of optical depth, gives:

$$I_\nu(0) = I_\nu\big(\tau_\nu(s)\big) e^{-\tau_\nu(s)} + \int_0^{\tau_\nu(s)} S_\nu\, e^{-\tau'_\nu}\, d\tau'_\nu. \tag{4.11}$$

Note that this expression is valid only when scattering is neglected. For an isothermal medium, S_ν is constant along the path, or, in other words, is independent of the optical depth. In this case, the formal solution of 4.11 simplifies to:

$$I_\nu(\tau_\nu) = I_\nu(0)\, e^{\tau_\nu} + S_\nu(T)\left(1 - e^{\tau_\nu}\right), \tag{4.12}$$

Equation 4.12 shows that, even with a constant source function, the emerging radiation intensity depends on the optical depth of the medium through the exponential factor, which describes the cumulative effect of emission and absorption along the path. In more general cases, variations in the source function across frequency, for example due to specific molecular constituents, can produce absorption or emission features in the observed spectrum. Three important limiting regimes can be identified:

1. **Optically thick medium ($\tau \gg 1$)**:
   When the optical depth is very large, the medium is highly opaque,

so the exponential term of Equation 4.12 approaches zero. Thus, the emerging intensity tends to

$$I_\nu(s) \approx S_\nu(T).$$

This means that the radiation observed is determined almost entirely by the local emission properties of the medium and is independent of the background radiation or the exact amount of material. If the medium behaves like a perfect blackbody, the source function corresponds to the Planck function $B_\nu(T)$, defined later in Equation 4.14. Observing optically thick emission therefore provides a direct measurement of the temperature of the emitting medium. The case when $S_\nu \neq B_\nu(T)$ will be discussed later.

2. **Optically thin medium ($|\tau| \ll 1$)**:
For very small optical depth values (optical depth close to zero), the material is absorbing little along the line of sight, and the exponential term of Equation 4.12 can be approximated by the first terms of its Taylor expansion, $e^{-\tau} \approx 1 - \tau$. This leads to

$$I_\nu \approx I_\nu(0)\,(1-\tau) + S_\nu(T)\,\tau. \tag{4.13}$$

In this case, the observed intensity depends linearly on the optical depth and thus on the amount of absorbing or emitting material along the line of sight. Emission or absorption becomes directly proportional to the column density of the gas, which makes this regime particularly valuable for analyzing and comparing atmospheric compositions. If locally the source function is smaller than the background intensity ($S_\nu(T) < I_\nu(0)$), absorption lines appear; conversely, if it is greater ($S_\nu(T) > I_\nu(0)$), emission lines are observed. Such optically thin spectral features allow to identify and quantify the specific atmospheric constituents by relating the intensity of the feature to the column density of the material.

3. **Negative optical depth ($\tau \ll -1$)**:
A negative optical depth corresponds to an amplifying medium, where the radiation intensity grows exponentially as it passes through. This is the regime of maser emission, which can produce extremely intense

and narrow spectral lines. Maser phenomena, however, are outside the scope of this thesis.

When the optical depth of a spectral line is around unity ($\tau \sim 1$), the interpretation becomes more complex, as the observed intensity depends on a combination of background radiation, emission, and absorption effects, and more importantly the column density and temperature of the medium. This intermediate regime is commonly encountered in molecular line observations of astrophysical media such as interstellar clouds and planetary atmospheres.

If the medium is in a state of Local Thermodynamic Equilibrium (LTE), the populations of atomic or molecular energy levels and the velocity distribution of particles can be described by a single local temperature. LTE occurs when collisions between particles dominate over radiative processes, so that excitation and de-excitation are effectively governed by the local kinetic temperature. Under these conditions, the level populations follow a Boltzmann distribution at the same temperature that defines the source function. Consequently, the source function S_ν depends only on this temperature T and equals the Planck function $B_\nu(T)$:

$$B_\nu(T) = \frac{2h\nu^3}{c^2} \frac{1}{e^{\frac{h\nu}{k_B T}} - 1}, \tag{4.14}$$

where h is Planck's constant, c is the speed of light, and k_B is Boltzmann's constant. This relation directly links the observed radiation to the local temperature under LTE conditions.

4.2 Spectral line theory

Observations of molecules and atoms are based on the analysis of spectral lines. These lines are produced when a molecule absorbs or emits photons through transitions between different energy levels. The photon energy correspond to the energy difference between the two levels $\Delta E = h\nu$.

A way to introduce the basic theory of spectral line is to consider a two-level system, a simple model of an atom or molecule. Particles can occupy either a lower state with energy E_1 or an upper state with energy E_2, thus separated by an energy gap $\Delta E = h\nu$, where h is Planck's constant and ν the transition frequency (see Figure 4.2). Transitions between the two levels occur through

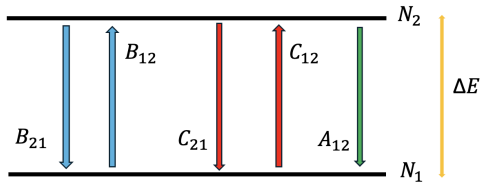

Figure 4.2: Schematic representation of a two-level system. The lower level is N_1 and the upper level is N_2, separated by the energy gap $\Delta E = h\nu$. Radiative and collisional processes are indicated: spontaneous emission (A_{21}), stimulated absorption (B_{12}), stimulated emission (B_{21}), collisional excitation (C_{12}), and collisional de-excitation (C_{21}).

four fundamental processes:

- *Spontaneous emission*: a molecule emits a photon when it transits from the upper energy level E_2 to the lower energy level E_1, in the absence of an external radiation field. The rate of spontaneous emission is proportional to the number density of molecules in the upper state n_2:

$$\frac{dn_1}{dt} = n_2 A_{21}, \tag{4.15}$$

  where A_{21} is the Einstein coefficient for spontaneous emission.

- *Stimulated absorption*: occurs when an atom in the lower state E_1 absorbs a photon with energy equal to the energy difference between the levels, $\Delta E = h\nu$. The absorption rate depends on the intensity of the external radiation field, I_ν, at the absorption frequency $\nu = \Delta E/h$, and on the population of the lower level n_1:

$$\frac{dn_2}{dt} = n_1 B_{12} I_\nu, \tag{4.16}$$

  where B_{12} is the Einstein coefficient of stimulated absorption.

- *Stimulated emission*: occurs when an incoming photon induces a molecule in the upper energy level E_2 to transition to the lower energy level E_1,

emitting a photon that has the same energy, direction, and phase as the incoming photon. The rate of stimulated emission is proportional to both the number of molecules in the upper energy level, n_2, and the intensity of the incoming radiation:

$$\frac{dn_2}{dt} = -n_2 B_{21} I_\nu, \tag{4.17}$$

where B_{21} is the Einstein coefficient of stimulated emission. The Einstein coefficients A_{21}, B_{21}, and B_{12} are intrinsic properties of the atom or molecule in question and are unique for each pair of energy levels.

- *Collisional excitation and de-excitation*: besides radiative processes, transitions between the two energy levels can also occur through collisions with other particles in the gas. These interactions can transfer kinetic energy to (or from) the molecule, leading to excitation from E_1 to E_2, or de-excitation from E_2 to E_1. The rate of collisional excitation is proportional to the number of molecules in the lower level, n_1, the density of collisional partners, n, and the collisional rate coefficient C_{12}:

$$\frac{dn_2}{dt} = n_1 \, n \, C_{12}. \tag{4.18}$$

  Conversely, the rate of collisional de-excitation is proportional to the number of molecules in the upper level, n_2, the density of collisional partners, and the corresponding de-excitation coefficient C_{21}:

$$\frac{dn_1}{dt} = n_2 \, n \, C_{21}. \tag{4.19}$$

  The collision coefficients not only depend on the intrinsic properties of the atom or molecule, but also on the nature of the collisional partner and on the kinetic temperature of the gas. If collisions dominate over the radiative process the system can be considered in LTE, where the level populations are given by Boltzmann distribution at this kinetic temperature.

If the two-level system is in a steady state, the processes involving upward and downward populations must be balanced. So we get:

$$N_1(\bar{I}_\nu B_{12} + nC_{12}) = N_2(\bar{I}_\nu B_{21} + nC_{21} + A_{21}), \tag{4.20}$$

where N_1 and N_2 are the total populations of the lower and upper levels, $\bar{I}_\nu$ is the average radiation intensity [W m^{-2} Hz^{-1}], and n is the number density of collision partners [cm^{-3}]. Under the assumption of LTE, it is straightforward to show that the Einstein coefficients are related by

$$B_{12} = \frac{g_2}{g_1} B_{21}, \quad A_{21} = \frac{8\pi h \nu_{21}^3}{c^2} B_{21}, \tag{4.21}$$

where g_1 and g_2 are the statistical weights of the lower and upper levels. These relations, first derived by Einstein (1917), hold generally, regardless of LTE or collisional effects. The relative populations of the two levels can be described by a Boltzmann distribution at the excitation temperature $T_{\rm ex}$:

$$\frac{N_2}{N_1} = \frac{g_2}{g_1} e^{-h\nu_{21}/kT_{\rm ex}}. \tag{4.22}$$

By definition, $T_{\rm ex}$ is the excitation temperature, which equals the kinetic temperature T_k under LTE. Collisional coefficients C_{12} and C_{21} depend on the collisional cross-section and the relative velocity of the molecules. They satisfy detailed balance at the kinetic temperature:

$$\frac{C_{12}}{C_{21}} = \frac{g_2}{g_1} e^{-h\nu_{21}/kT_k}. \tag{4.23}$$

From the steady-state condition (Equation 4.20), one can also write

$$\frac{N_2}{N_1} = \frac{I_\nu B_{12} + nC_{12}}{A_{21} + I_\nu B_{21} + nC_{21}}. \tag{4.24}$$

Using the above relations for the transition coefficients, Eq. 4.21 and Eq. 4.23 and assuming the radiation intensity is that of a blackbody at temperature T (Eq. 4.14) this simplifies to

$$\frac{N_2 g_1}{N_1 g_2} = \frac{A_{21} J(T) + nC_{21} e^{-h\nu_{21}/kT_k}}{A_{21}(1 + J(T)) + nC_{21}}, \tag{4.25}$$

where $J(T) = 1/(e^{h\nu/kT} - 1)$. This relation links the level populations to the gas density, kinetic temperature, and radiation field. Using the definition of

$T_{\rm ex}$ from Eq. 4.22, we find:

$$\frac{h\nu_{21}}{kT_{\rm ex}} = \ln\left[\frac{A_{21}\left(1+J(T)\right)+nC_{21}}{A_{21}J(T)+nC_{21}e^{-h\nu_{21}/kT_k}}\right]. \tag{4.26}$$

This equation shows how the population distribution is related to the density and kinetic temperature of the gas, and the equivalent temperature of the radiation field. Two limiting cases are particularly interesting:

- For $n \to 0$, radiative and spontaneous processes dominate, and the population distribution becomes thermalised at the radiation field temperature ($T_{\rm ex} \to T$).

- For $n \to \infty$, collisions dominate and the population distribution becomes thermalised at the kinetic temperature of the gas, leading to LTE ($T_{\rm ex} \to T_k$).

When collisional de-excitation dominates, the density at which this occurs is defined by the *critical density*:

$$n_{\rm crit} = \frac{A_{21}(1+J(T))}{C_{21}}. \tag{4.27}$$

For high-frequency transitions where $h\nu \gg kT$, the contribution of the radiation field $J(T)$ is negligible, so the expression simplifies to:

$$n_{\rm crit} \approx \frac{A_{21}}{C_{21}}. \tag{4.28}$$

This represents a lower limit and a rough estimate of the gas density at which LTE conditions may apply.When the local density is below $n_{\rm crit}$, collisional processes are insufficient to maintain a Boltzmann distribution of the level populations. As a consequence, the excitation temperature departs from the kinetic temperature, and the system must be treated in non-LTE. This situation is typical for tenuous planetary atmospheres and cometary comae, where densities are well below the critical values for water transitions.

The level populations can be connected to radiative transfer equation 4.12 through the emission and absorption coefficients:

$$\epsilon_\nu = N_2 A_{21} h\nu\phi(\nu_{21}), \quad \kappa_\nu = (N_1 B_{12} - N_2 B_{21}) h\nu\phi(\nu_{21}), \tag{4.29}$$

where $\phi(\nu_{21})$ is the line profile function, which describes the distribution of photon frequencies around the transition. The width of the line is determined by several broadening mechanisms, including natural broadening, thermal Doppler broadening, and collisional (pressure) broadening. Through Eq. 4.29, 4.21 and 4.22, the optical depth along the line of sight depends on the column density of molecules in the upper level, $N_{c,2} = \int N_2 \, ds$:

$$\tau_\nu = \frac{c^2}{8\pi\nu^2} N_{c,2} A_{21} \left(e^{h\nu/kT_{\rm ex}} - 1 \right) \phi(\nu_{21}). \tag{4.30}$$

In reality, a two-level system is rarely found in nature, except in environments where all particles reside in their ground state. Therefore, the spectral line theory must be generalized to multi-level systems. In such systems, the population distribution can often be described by a single excitation temperature $T_{\rm ex}$, and the column density N_u in the upper level of a given transition is related to the total column density $N_{\rm tot}$ through the *partition function* $Q(T_{\rm ex})$:

$$N_u = \frac{g_u}{Q(T_{\rm ex})} \, e^{-E_u/kT_{\rm ex}} \, N_{\rm tot}, \tag{4.31}$$

where the partition function $Q(T_{\rm ex})$ represents the sum over all possible energy levels, weighted by their degeneracy g_i and Boltzmann factor:

$$Q(T_{\rm ex}) = \sum_i g_i \, e^{-E_i/kT_{\rm ex}}. \tag{4.32}$$

Intuitively, $Q(T_{\rm ex})$ accounts for how the total population is distributed among the available energy levels at a given excitation temperature. For linear molecules, the partition function can be approximated as

$$Q(T_{\rm ex}) \approx \frac{kT_{\rm ex}}{hB}, \tag{4.33}$$

where B is the rotational excitation constant of the molecule, see the following section for details.

4.3 Rotational transitions of molecules

Molecules possess internal degrees of freedom in addition to their electronic structure. In particular, they can undergo quantized *rotational*, *vibrational*, and *electronic* transitions, each producing characteristic spectral signatures across different regions of the electromagnetic spectrum.

- **Rotational transitions** occur when the molecule changes its rotational state. They are typically observed in the millimeter and sub-millimeter range, making them particularly relevant for radio and far-infrared astronomy.
- **Vibrational transitions** correspond to oscillations of the atoms around their equilibrium positions within the molecule (e.g., stretching or bending of chemical bonds). These transitions occur mainly in the infrared domain.
- **Electronic transitions** involve excitation of electrons to higher energy orbitals and require much larger energies. As a result, they are observed at optical and ultraviolet wavelengths.

The total excitation energy of a molecule can therefore be expressed as the sum of its contributions from rotational, vibrational and electronic excitation energies:

$$E_{\text{tot}} = E_{\text{elec}} + E_{\text{vib}} + E_{\text{rot}}. \tag{4.34}$$

with:

$$E_{\text{rot}} \ll E_{\text{vib}} \ll E_{\text{elec}}. \tag{4.35}$$

Although rotational energies are much smaller than electronic energies, they are constrained by the overall electronic state. For water, the ground electronic state is closed-shell, so rotational transitions can be studied largely independently. For water, this enables the study of rotational spectra in the millimeter and sub-millimeter ranges. These spectral lines are important for interpreting planetary atmospheres and for astronomical observations, as they provide direct information about the rotational motions of the molecules without involving higher-energy electronic excitations.

The simplest model to describe rotational motion in molecules is the *rigid rotor* approximation, which assumes fixed bond lengths and neglects vibra-

tional motion. The rotational energy of a rigid rotor is given by:

$$E_{\text{rot}} = \frac{L^2}{2I}, \tag{4.36}$$

where L is the total angular momentum and I is the moment of inertia of the molecule around its rotation axis.

Following quantum mechanics, the angular momentum of a molecule is quantized and given by:

$$L = \hbar\sqrt{J(J+1)}, \tag{4.37}$$

where $J = 0, 1, 2, \ldots$ is the rotational quantum number and $\hbar = h/(2\pi)$ is the reduced Planck constant. Substituting this expression in the energy formula (Eq. 4.36) yields:

$$E_{\text{rot}} = \frac{\hbar^2}{2I} J(J+1). \tag{4.38}$$

It is convenient to define the *rotational constant* B to simplify notation:

$$B = \frac{\hbar^2}{2I} \tag{4.39}$$

The rotational energy can then be written compactly as:

$$E_J = BJ(J+1), \tag{4.40}$$

with energy in Hz or cm^{-1} depending on the units of B.

Diatomic molecules: CO, H_2, N_2

Diatomic molecules, such as CO, can undergo quantized rotational transitions when interacting with electromagnetic radiation. In the case of molecules with a permanent electric dipole moment, like CO, these transitions are *electric dipole transitions*, meaning that the molecule can emit or absorb a photon while changing its rotational quantum number.

The selection rules for dipole-allowed rotational transitions are:

$$\Delta J = \pm 1, \tag{4.41}$$

where J is the rotational quantum number.

For CO, which has a rotational constant $B_0 \sim 57$ GHz, the frequency of

the $J \to J-1$ rotational transition is given by:

$$\nu(J \to J-1) = 2B_0 J. \tag{4.42}$$

Molecules without a permanent dipole moment, such as H_2 or N_2, cannot undergo dipole-allowed rotational transitions. In those cases, only much weaker processes, such as quadrupole transitions, are possible.

Non-linear molecules: H_2O

The rotational properties of *non-linear* molecules can be characterised using the *moment of inertia tensor* $\mathbf{I}$. By choosing a coordinate system centered at the molecule's center of mass that rotates along with the molecule, the tensor can be written as a diagonal matrix:

$$\mathbf{I} = \begin{pmatrix} I_a & 0 & 0 \\ 0 & I_b & 0 \\ 0 & 0 & I_c \end{pmatrix}, \tag{4.43}$$

where I_a, I_b, and I_c are the projections of moments of inertia along the corresponding axes (Gordy et al., 1984; Hollas, 1998; Yamamoto, 2017). Molecules can be classified according to their rotational symmetry.

- **Spherical tops:** $I_a = I_b = I_c$; these molecules have three equivalent axes of symmetry. In the rigid rotor approximation, spherical tops have no permanent dipole moment and therefore do not exhibit observable rotational spectra.
- **Symmetric tops:** molecules with a single axis of rotational symmetry. They can be further divided into:
  - **Prolate symmetric tops:** $I_c = I_b > I_a$ (elongated along a)
  - **Oblate symmetric tops:** $I_c > I_b = I_a$ (flattened along c)
- **Asymmetric tops:** all three principal moments of inertia differ, $I_a \neq I_b \neq I_c$, as in the case of H_2O. For these molecules, the total energy and angular momentum are conserved, but not the projection of the angular momentum along any symmetry axis, making the rotational spectrum more complex.

The spectroscopic notation of water borrows from the symmetric top formalism. Rotational states are conventionally labeled as J_{K_a,K_c}, where K_a and K_c denote the limiting cases of projection along the a (prolate) and c (oblate) principal axes, respectively. The electric dipole selection rules for H_2O are:

$$\Delta J = 0, \pm 1, \quad \Delta K_a, \Delta K_c = \pm 1, \pm 3. \tag{4.44}$$

In addition, water, like molecular hydrogen, exists in two nuclear spin isomers:

- **Ortho-H_2O:** parallel proton spins (total nuclear spin $I = 1$),
- **Para-H_2O:** antiparallel proton spins (total nuclear spin $I = 0$).

These two species are spectroscopically distinct, since radiative transitions between ortho and para states are forbidden, and thus they behave as separate molecular species .Water has a large number of allowed rotational transitions at far-infrared and millimeter wavelengths. In planetary atmospheres and interstellar gas, these transitions can play an important role in radiative cooling, although at high densities line trapping may reduce their efficiency (Neufeld et al., 1995; Dishoeck, 2013).

As an example, Figure 4.3 illustrates the energy level structure of H_2O with some of the main rotational transitions observable from space-based telescopes. In particular, the ground-state ortho-H_2O transition at 557.936 GHz ($1_{10} \rightarrow 1_{01}$), that is the focus of Paper I, is highlighted in red. This low-excitation line is a highly sensitive tracer of cold, low-density water vapor, especially for tenuous atmospheres of icy moons, due to its relatively high Einstein A_{21} coefficient and the low column densities expected. Observing this transition from the ground is very challenging because atmospheric water vapor strongly attenuates the signal. For this reason, space-based instruments such as the SWI onboard JUICE have been specifically designed to target this line for studies of Ganymede's atmosphere.

In icy moon atmospheres, collisional processes with H_2 and with H_2O molecules themselves are crucial to populate the rotational levels and to drive the excitation of sub-millimeter transitions. In non-LTE conditions, which are typical of tenuous atmospheres, collisional excitation and de-excitation must be explicitly taken into account when modeling the water spectrum. The 557.936 GHz line, in particular, is highly sensitive to these processes. For densities below the critical density of the transition, collisions are not suffi-

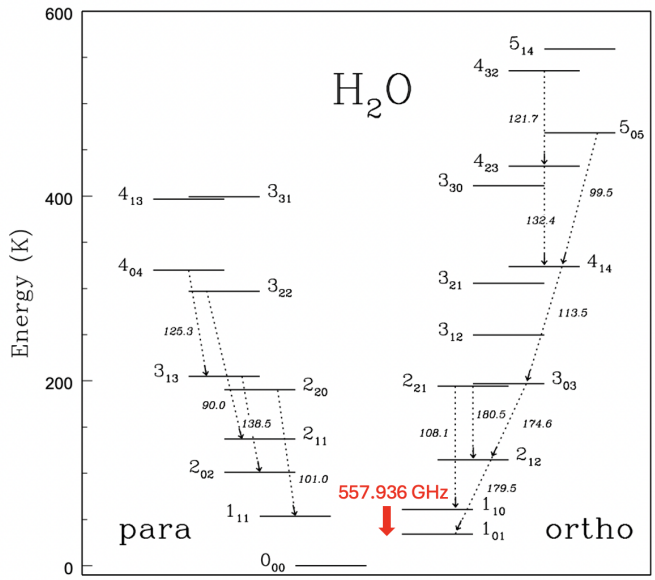

Figure 4.3: Energy level diagram of H_2O showing rotational transitions occurring for both para and ortho species. Wavelengths are indicated in microns. The ground-state ortho-H_2O line at 557.936 GHz ($1_{10} \rightarrow 1_{01}$) is highlighted in red. **Credit**: adapted from Nisini et al. (1999)

cient to thermalize the levels, and the excitation temperature departs from the kinetic temperature.

Throughout this thesis, the modeling of Ganymede's water emission therefore relies on a non-LTE treatment, as LTE assumptions would systematically underestimate the role of radiative processes.

CHAPTER 5

The LIME code

LIME (Lime Modeling Engine) is a versatile excitation and radiative transfer code designed to predict both line and continuum radiation from an astronomical source model in non-LTE. Unlike many traditional radiative transfer codes that are restricted by cylindrical or spherical symmetry, LIME is able to model complex and arbitrary 3D geometries, making it highly flexible and applicable to a wide range of astrophysical problems. It employs unstructured Delaunay grids for photon transport, combined with accelerated Lambda iteration for calculating level populations. Originally developed by Brinch et al., 2010, the latest release of LIME is version 1.9.5, which was made available in 2018. Although originally designed for protoplanetary disks and star-forming regions, we adapted the code for planetary atmospheres[1].

In this chapter, I will outline the computational procedure used in LIME for performing radiative transfer simulations, which is described in detail in the manual[2]. The process begins by generating an unstructured Delaunay grid through random sampling of the input model. The code then iteratively calcu-

[1] Modifications include changes in the density and temperature profiles, the geometry of the computational domain.

[2] https://lime.readthedocs.io/en/latest/usermanual.html

lates the rotational level populations at each grid point, considering local parameters such as temperature, density, and radiation field. Finally, LIME performs ray-tracing of the model, generating a comprehensive data cube that is output in FITS (Flexible Image Transport System) format, the standard data format in astronomy for storing and transferring multi-dimensional datasets (Pence et al., 2010). Figure 5.1 provides an overview of the consecutive steps of the procedure, including inputs and outputs, intended as a guide through the following detailed descriptions.

5.1 The Computational Procedure

To simulate the observed spectral line radiation of an astronomical object, we need to make use of an astronomical source model. The purpose of the source model is to numerically represent the geometrical and physical structure of the astronomical source, which allows us to simulate the observed spectral line radiation. The source model is written in C and compiled together with LIME at runtime, and for simplicity, we will refer to the model file as `model.c`. This file contains the necessary numerical parameters to create the structure of the model and the molecular data files. Specifically, it includes input functions, files and parameters that will be described here below.

Input

First of all, I will introduce the input functions that define the physical properties of the gas in the model. In this work, these properties are described analytically as functions of the x, y, z coordinates, allowing for a flexible representation of the geometry of the source and its physical properties in three dimensions. Although LIME supports this analytical approach, it is also possible to provide data from numerical simulations – such as MHD models – by or from tabulated data grids by implementing appropriate interpolation routines. The analytical functions are:

- **Density distribution**: the 3D density distribution of the main collision partner(s), where the density is expressed as the number density (i.e., the number of collision partners per unit volume, in cubic meters). This profile determines how the dominating gas component(s) is distributed in the modeled region.

- **Temperature distribution**: the kinetic gas temperature (in Kelvin) described by a 3D spatial distribution across the model domain. This distribution is crucial for determining the excitation of molecules.
- **Molecular abundance distribution**: This defines the fractional abundance of the gas species of interest with respect to the primary collision partner. The density of a species is then given by the product of its abundance and the density of the primary collision partner.
- **Random velocity**: describes the velocity dispersion of the random motions of the gas. This is characterized by the Doppler b-parameter, which represents the 1/e half-width of the line profile. It is typically a scalar but can also be entered as a 3D distribution.
- **Velocity field**: a 3-component vector (v_x, v_y, v_z) distribution representing the velocity components of the gas in the x, y, and z directions. This is important for simulating the kinematic properties of the gas.
- **Gas-to-dust ratio**: the ratio between the number density of gas and dust particles, which is used in the model to account for the emission and absorption of dust in calculating the local mean radiation field.

To reproduce the astronomical source, it is necessary to include also the molecular data file of the gas to be simulated. These files contain important molecular properties such as energy levels, Einstein coefficients, and collisional rates, which are needed for the excitation and radiative transfer calculations. The user will then select, as other inputs of the model, the specific molecular transitions to be modeled, as well as the spatial and spectral resolution for the output.

Furthermore, the `model.c` file contains the input numerical parameters that describe the structure of the model and define the computational domain. Some of the most relevant parameters are listed below:

- **Outer radius of the computational domain**: This parameter defines the size of the modeled region and must be set large enough to cover the entire spatial extent of the model.
- **Total number of grid points**: This specifies the number of points used to discretize the 3D domain. The resolution of the grid directly

affects the precision of the model. Additionally, the more property discontinuities the model has, the more grid points are required to maintain a sufficient level of precision in the simulation.

- **Number of sink points**: This refers to the number of grid points on the surface of the model, which is important for defining the boundary conditions and the interaction of radiation with the surface.

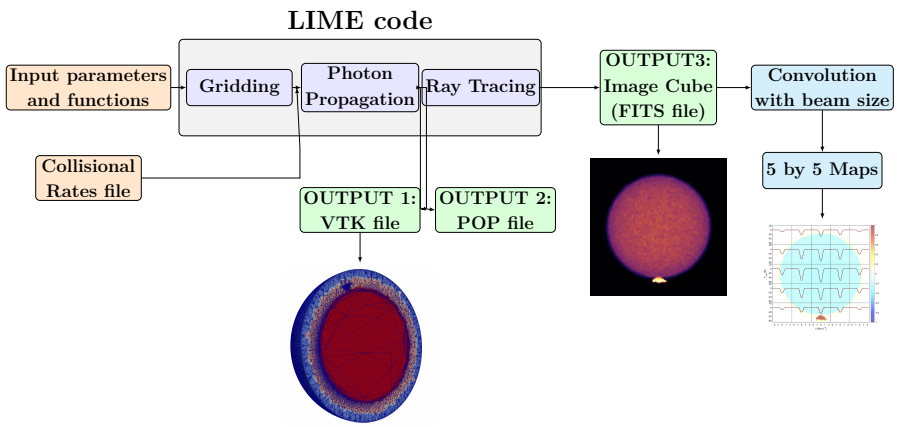

Figure 5.1: The computational workflow of the LIME code. Starting from input parameters and functions, the code generates a 3D Delaunay grid (Gridding step). Using a molecular data file – which includes both spectroscopic data (such as energy levels and Einstein coefficients) and collisional rate coefficients – it then simulates photon propagation with iterative level population calculations, followed by ray-tracing to produce a spectral image cube in FITS format. Additional outputs include the grid structure in VTK (Visualization Toolkit) format (Schroeder et al., 2006) and population data files (POP files). Finally, the image cube is convolved with the instrument beam to produce water spectral lines overlaid on moment-zero maps (integrated intensity) suitable for comparison with observations.

Gridding

Once the `model.c` file is ready and the input functions are set, the next step is to run the LIME code. In the LIME procedure, a random set of points representing the local environment (density, temperature, population,radiation field, etc) is distributed in 3D space. These grid points are placed randomly throughout the entire computational domain. In this work, the gridding is weighted by the density profile of the source model, which is used as a probability distribution for the placement of the points. This results in an average distance between neighboring points that is inversely proportional to the local density, and approximately proportional to the mean free path, $l = \alpha \times \mathrm{n}^{-1}$, where α is the relevant collision parameter. Alternative weighting schemes—e.g., based on temperature or opacity—are also possible in LIME.

When the point distribution has been generated, the points are connected by *Delaunay triangulation*. Delaunay triangulation connects points in such a way that no point falls inside the circumsphere of any triangle (or tetrahedron in 3D) formed by neighboring points, see left panel of Fig. 5.2. While Delaunay triangulation is used to define the paths along which photons travel during the radiative transfer calculations, the actual physical space associated with each point is described by the corresponding *Voronoi cell*, see as example in panel right of Fig. 5.2. The Voronoi diagram divides the entire 3D domain into separate, non-overlapping volumes – each associated with one grid point – within which physical properties such as density, temperature, and molecular abundance are assumed to be constant. These Voronoi cells are used during ray-tracing, when photons are integrated along straight paths through the model.

During the gridding process of our source model, LIME also distribute a set of points randomly on the surface of a sphere surrounding the computational domain. These surface points are included in the triangulation and linked to the internal grid points. However, they don't represent anything except the surface of our computational domain. Whenever a photon reaches one of these surface points, it is considered to have escaped the model, marking the end of its trajectory.

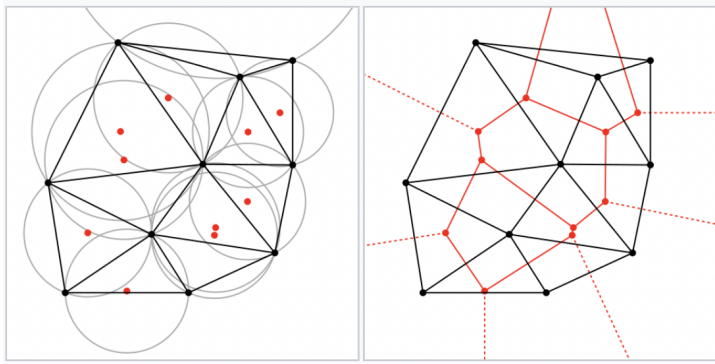

Figure 5.2: On the left panel, the Delaunay triangulation with all the circumcircles and their centers (in red) is shown. Connecting the triangulation's circumcenters gives the Voronoi diagram (in red), illustrated in the left panel. **Credit**: Wikipedia Commons

Photon propagation

With the gridding and Delaunay triangulation in place, LIME proceeds to simulate the propagation of photons through the model domain in order to compute the radiation field and molecular excitation. Photon transport in LIME occurs along the Delaunay connections between grid points. On average, each point is connected to about 16 neighbors (Ritzerveld & Icke 2006), which limits the spatial sampling of the radiation field J_ν to this number of directions.

Due to the random orientation of the Delaunay lines, photons cannot travel in perfectly straight paths across the grid. To approximate directional propagation, at each grid point the photon continues along one of the two outgoing lines forming the smallest angle with the original direction. The choice is made probabilistically, weighted by the relative angle. As a result, the photon trajectory deviates slightly at each step, forming an overall cone around the initial propagation direction. The resulting angular distribution has been described as approximately Gaussian. However, this is only an approximation: the actual distribution depends on the gridding and interpolation scheme, and may lead to deviations from ideal directional transport, especially in regions with strong gradients or anisotropic structures. This behavior has been

subject to discussion, particularly when comparing versions 1.4 and 1.9.5 of LIME, although a detailed quantitative assessment is still lacking.

Points located in high-density regions tend to have more Delaunay connections in our model, because the grid point distribution is weighted by the local density. This choice results in a gridding structure where the local optical depth τ scales inversely with density, as desired to reproduce a mean free path that reflects the physical conditions of the medium. It should be noted that alternative gridding strategies could lead to different connectivity patterns.

LIME integrates the radiative transfer equation all the way to the boundary of the computational domain, where the external contribution – typically the cosmic microwave background – is added. This is known as the method of *long characteristics*, (Mihalas, 1978). The radiation field J_ν and the level populations n_i are coupled through the transfer equation and are solved iteratively. The initial estimate assumes Local Thermodynamic Equilibrium (LTE) and a black-body radiation field, so the non-LTE and combined radiation field from dust and molecules are only considered from the second iteration. The iterative solution adopted in LIME resembles the Accelerated Lambda Iteration (ALI) scheme, in which the radiation field is separated into local and external contributions to improve convergence speed and stability. This approach avoids explicitly building the full Λ matrix and instead approximates the solution by solving for the radiation field within each Voronoi cell using the populations from the previous iteration.

The iterative solution requires a convergence criterion to determine when the level populations and radiation field have stabilized. In LIME, this can be handled in different ways depending on the version and user setup. One common approach is to fix the number of iterations (e.g., 14–20), assuming that convergence will be sufficiently achieved by then. Alternatively, a more dynamic criterion could be implemented to monitor changes in level populations between successive iterations and stop the calculation once a user-defined threshold is reached. In this work, we adopted the former approach, specifying a fixed number of iterations.

Ray-tracing

Once the iterative solution has converged, LIME proceeds to ray-trace lines of sight through the model to generate an image cube of the escaping radiation.

The user specifies the source distance, relative velocity, orientation, image resolution, and units. Unlike simpler 2D codes that only require inclination and position angle, LIME allows full 3D viewing by including a rotation angle, enabling visualization of the model from any direction using a rotation matrix.

In the ray-tracing stage, photons propagate along straight lines through the model domain, rather than following the Delaunay connections used during the Monte Carlo iterations. This approach is common across LIME versions and makes use of the Voronoi diagram to determine the physical conditions encountered by the photons. Each Voronoi cell is assumed to have uniform properties based on its associated grid point, and the radiative transfer equation is integrated step-by-step through the volume, as the ray passes through successive cells.

Output files

The grid. Once the Delaunay grid has been constructed by LIME (see Fig. 5.1), the code generates a VTK file containing the grid structure and the associated physical properties specified in the input. This file can be read using various visualization software packages, for example, ParaView[3], an open-source program available for multiple platforms.

The grid file includes the (x, y, z) coordinates of each grid point and information about its neighboring points, allowing the Delaunay grid to be fully reconstructed. It also contains three scalar fields – H_2 density, temperature, and molecular abundance – and a vector field representing the velocity.

Visualizing the grid in ParaView can be a useful way to verify that the model behaves as expected and that the point distribution matches the physical structure of the source. An example of the grid generated for the Ganymede atmosphere model is shown under the panel *OUTPUT 1* in Fig. 5.1.

Populations. The level populations resulting from the photon propagation (see Fig. 5.1) are saved in a separate output file with the `.pop` extension. This file includes the (x, y, z) coordinates of each grid point along with the H_2 density, temperature, molecular abundance, and the computed level populations. Unlike the VTK grid file, it does not contain information about the neighbors of each point, so the Delaunay triangulation cannot be reconstructed from it. However, the population file is useful for plotting 2D projections or slices of the physical and excitation properties of the model.

[3] `https://www.paraview.org/`

Images cubes. After the ray-tracing step, LIME outputs the image cube of the model in the standard FITS format. This file contains the spectral and spatial information of the escaping radiation for the selected source distance and viewing angle and can be analysed using any standard FITS viewer. An example is CARTA (Cube Analysis and Rendering Tool for Astronomy), a next-generation tool for image visualization and analysis (Comrie et al., 2021). An illustration of how a FITS file can be inspected in CARTA is shown in Fig. 5.1, below the panel *OUTPUT 3*. The figure displays the simulation of Ganymede's atmosphere with a water plume located at the south pole, corresponding to the same model previously shown to the right of the panel *OUTPUT 1: VTK file*.

5.2 Generating spectral maps for analysis

Although LIME lets users set the output image resolution via pixel size, it does not allow to internally convolve the image with a specific instrumental beam by default. Thus, the FITS file typically contains a high-resolution, unconvolved image cube. Moment-zero maps can be generated from these cubes by integrating the spectral line intensity over the velocity axis, which are used for spectral analysis and model interpretation.

To simulate realistic telescope observations, the high-resolution cubes must be convolved externally with the instrument beam using dedicated software. A common method is to convolve the image cube with a 2D Gaussian beam by making use of MATLAB[4], Python[5] or other software. After convolution, spectral maps of arbitrary size (e.g., a 5×5 pixel grid) can be extracted from the convolved cube for detailed spectral and spatial analysis. This process facilitates direct comparison with observational data and assists in interpreting spectral features. An example is shown in Fig. 5.1 on the right panel, which displays the baseline-subtracted water spectra overlaid on a moment-zero map (integrated intensity). In the map, regions ranging from light cyan to dark blue correspond to increasing absorption, while regions ranging from light yellow to dark red correspond to increasing emission. The water plume is clearly visible at the south pole.

[4] `https://www.mathworks.com`
[5] `https://www.python.org/`

CHAPTER 6

Radiative transfer models of Ganymede's water atmosphere

The main goal of this thesis (and Paper I) is to investigate whether water plumes in Ganymede's atmosphere can be detected by the Submillimetre Wave Instrument (SWI) during the JUICE mission's planned moon-monitoring observations. Ganymede's water atmosphere is expected to be highly inhomogeneous: if water sublimation from the icy surface is the dominant source, the water distribution will not be radially symmetric but rather concentrated at low altitudes near the sub-solar point. Additionally, collisional excitation of water molecules is efficient only in the densest regions near the sub-solar point, while at higher altitudes and larger angular distances from this point, excitation becomes dominated by radiative processes. Therefore, the spectral lines observed by SWI will arise from a strongly non-local thermodynamic equilibrium (non-LTE) regime, making accurate modeling essential for interpretation. In this context, a 3D non-LTE radiative transfer approach is required to reproduce the expected line profiles. This approach becomes even more important if aiming to model the effect of a localized water plume that can be situated at any angle away from the SSP, adding significant asymmetry to the atmospheric structure. For this reason, LIME was selected to simulate

water signatures from Ganymede's atmosphere

To apply LIME to the Ganymede case, we used the atmospheric water source model described by Wirström et al. (2020), which is based on analytical simplifications of the theoretical results from Marconi (2007) on Ganymede's atmospheric composition and structure (see Section 2.2 for details). The approach to achieve the goal of this thesis is to compare a sublimation-dominated water atmosphere model based on Wirström et al. (2020) with the same model including a localized plume, which was developed as part of this study. In Paper I, we also investigate how changes in plume properties influence the detectability of the water signatures, varying one parameter at a time while keeping the others constant.

Before presenting the plume model, it is useful to first briefly review the most important aspects of the Wirström et al. (2020) model, which forms the basis of Ganymede's sublimation-dominated water atmosphere and the starting point for the modifications made in this study:

- **General geometry**
  The model uses a spherical domain centered on Ganymede, with a total radius of 3500 km. The surface of Ganymede is defined at a radius of 2634 km, and the atmosphere extended up to an altitude of 450.5 km. For the Delaunay grid, a total of 100 000 grid points were chosen, a number verified to be sufficient through convergence testing: reducing the number of points by a factor of two affected the resulting line profiles by less than 0.5%. Grid sampling optimisation is described in the dedicated subsection 6.2.

- **Water parameters**
  The source model by Wirström et al. (2020) consists of vertical distributions of water number density and temperature, extending from the surface up to approximately 450 km altitude. These distributions are set to vary with the angular distance from the sub-solar point, with both density and temperature reaching their maxima near the sub-solar point. Figure 6.1 shows the vertical distributions used in the simulation, taken from Wirström et al. (2020). The dashed lines represent the water number density and the solid lines the temperature profiles, for different angular distances from the SSP. The upper and lower curves correspond to the maximum and minimum atmospheric boundaries, respectively.

It is important to note that the water number density exceeds the critical density of the 557 GHz transition ($\sim 10^8$ cm^{-3}, see section 4.2) only in regions very close to the sub-solar point. For this reason, non-LTE conditions prevail throughout most of the atmosphere.

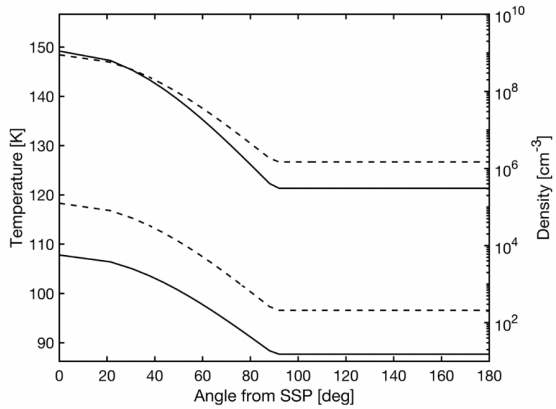

Figure 6.1: Vertical distribution of water density (dashed lines) and temperature (solid lines) used as input in the LIME model of Ganymede's atmosphere by Wirström et al. (2020). The profiles are shown as a function of altitude for different angular distances from the sub-solar point (SSP), with higher densities and temperatures near the SSP. The upper and lower curves represent the maximum and minimum atmospheric boundaries, respectively.

- **Molecular data**
  The LIME simulations compute the full excitation of water molecules, taking into account all energy levels and the balance between collisional and radiative processes under non-LTE conditions. Molecular parameters, including spectroscopic constants, transition frequencies, Einstein coefficients, and collisional rate coefficients, are taken from the LAMDA database. Water–water collisional rates are adopted from Buffa et al. (2000), and the ortho-to-para ratio is assumed to be the thermal equilibrium value of 3. While LIME calculates the excitation of all levels, the results are here extracted, presented, and analyzed specifically for the ortho-H_2O $1_{10} \rightarrow 1_{01}$ transition at 556.936 GHz.

- **Velocity field**
  The base model assumes a static velocity field, as vertical and horizontal velocities in Ganymede's lower atmosphere are expected to be below 100 m s^{-1} (Marconi, 2007). Therefore, the Doppler parameter is set to zero. The model is iterated 14 times to reach convergence in the level populations, with a convergence threshold of 10^{-3} between successive iterations.

6.1 LIME Versions Comparison: 1.4 vs 1.9.5

The version of LIME used in Wirström et al. (2020) was 1.4. However, the code has undergone improvements in recent years and the most recent publicly available version, 1.9.5, includes several updates to the ray-tracing module as well as the implementation of multithreading support to enhance performance. Minor adjustments also have been made to the gridding routines, although the overall structure remains consistent with earlier versions.

During the first year of my PhD, I verified that the atmospheric model of Wirström et al. (2020) could be reliably reproduced using the latest version of LIME. This involved re-running the same sublimation-dominated model originally computed with LIME 1.4, and comparing the results with those obtained from the updated version 1.9.5. To ensure the suitability of the updated version for modeling planetary atmospheres, systematic functional tests were performed to confirm that it could reproduce the results of the earlier version while potentially offering improvements in accuracy and performance. A full list of changes between versions is not available for LIME, as earlier releases (e.g., v1.4) are not hosted on GitHub. For readers interested in the development and updates of the code, we refer to the LIME GitHub repository: `https://github.com/lime-rt/lime`.

To compare the two versions more directly, we ran the same Ganymede atmospheric model with both 1.4 and 1.9.5. The results confirm that version 1.9.5 reproduces the main results of 1.4, while producing a better-structured Delaunay grid and more accurate sampling of the input functions, especially in high density regions such as the sub-solar point where values vary rapidly (see Fig 6.2). Differences in the gridding algorithm also lead to slightly improved convergence behavior in the radiative transfer calculations for the latest version. During the simulation runs and result comparison, it was observed that

the model in 1.9.5 is rotated by 180° compared to the 1.4 version. This affects the interpretation of the sub-solar point orientation in ray-traced images. To ensure consistency with earlier results, simulations in 1.9.5 must be configured with a viewing angle of 180°.

In Fig. 6.2, 5×5 moment-zero maps (see section 5.2 for details) generated from the two different LIME versions are shown. The maps display baseline-subtracted spectra overlaid on a moment-zero map (integrated intensity). In the moment-zero map, regions shaded from blue to dark blue indicate increasing absorption. The moment-zero map is shown at full resolution, with each pixel representing 6 arcsec. The spectral lines were obtained after convolving the model FITS image cube with the SWI beam, which has a full width at half maximum (FWHM) of 440 arcseconds. Noticeable variations in absorption depth are observed across Ganymede's disc, with the strongest absorption (up to 60 K) located near the sub-solar point (SSP) in the nadir direction.

The scenario shown corresponds to the case in which SWI is positioned directly above the SSP, i.e. at 0° phase angle. The left panel shows the output from version 1.9.5, while the right panel displays the same atmospheric model computed with version 1.4, as used in Wirström et al. (2020).

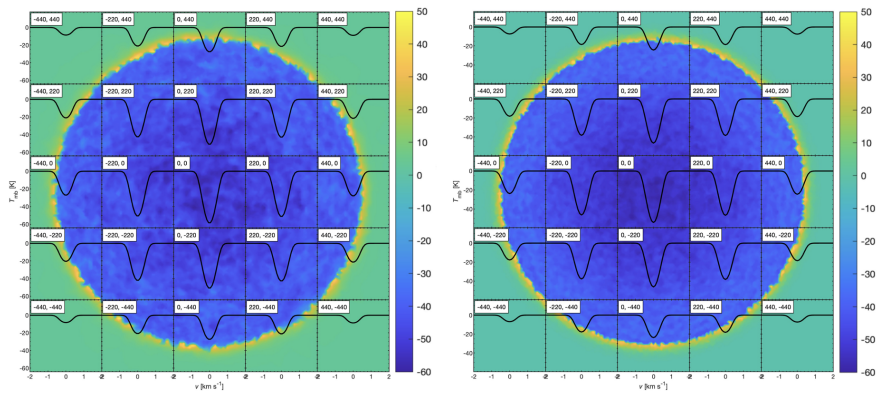

Figure 6.2: Results comparison for latest version of LIME 1.9.5 (left) and previous version 1.4 (right). Both use the same atmospheric input model, but differ in grid structure and radiative transfer behavior due to code updates.

6.2 Model development

Applying LIME v 1.9.5 to model spectral signatures from Ganymede's water atmosphere with and without a plume required several testing and modification steps, particularly related to grid optimization and the implementation of additional features such as localized water plumes.

Optimization of Grid Sampling in LIME

Generating an effective grid in LIME requires careful tuning of two key parameters: the total number of grid points and the number of sink points (i.e., surface points). The difference between these two determines the number of points distributed within the model volume, which are responsible for sampling the input physical quantities, such as density and temperature. For example, if 10000 total grid points are used and 3000 are assigned as sink points, only 7000 points remain to cover the model volume.

To ensure a finer sampling in regions where physical properties – such as density and temperature – exhibit stronger gradients, especially near the sub-solar point, we configured the grid so that the sampling probability in general is weighted based on the local gas density. We adopted an overall weighting function of the form $(n/n_0)^{0.2}$, where $n_0 = 10^9\,\mathrm{cm}^{-3}$ is a reference density. This approach increases the likelihood of placing grid points in denser regions, but since the densest region is the moon's interior, further modifications are required to avoid overpopulating it.

Another LIME key parameter controlling the distribution of the points is `minScale`, which differs between the two LIME versions. In LIME 1.4, `minScale` defines the minimum allowed distance between two grid points, effectively setting the smallest scale sampled in the model and it is expressed in meters. If `minScale` is set too small (e.g., 100 m or 10 m), the sampling becomes overly concentrated where the density is higher, typically near the center of the model (of the moon). As a result, the outer regions closer to the surface become under-sampled, leading to a poorly resolved and unbalanced grid that can negatively affect the convergence and accuracy of the simulation. Conversely, if minScale is too large, grid points become too sparsely distributed, especially in regions of strong gradients such as the sub-solar point, which again degrades the spatial resolution and reliability of the radiative transfer solution.

In contrast, LIME 1.9.5 redefines the `minScale` parameter as the minimum radius from the center of the moon from which grid points can be generated. This acts as an inner boundary of the grid domain. In our simulations, `minScale` has been set to 2500 km, corresponding to 84 km beneath the surface of Ganymede. To prevent unnecessary points from being placed deep inside the moon—where no emission is expected—we further reduced the sampling weight to 10^{-10} for radii smaller than 2550 km. This approach, together with the general sampling probability based on gas density described above, ensures that most of the grid points are placed in the denser atmospheric regions, allowing for improved spatial resolution where it is most needed without overpopulating the model center, while still preserving a sufficient number of points just below the surface to properly sample the sharp density gradient at the surface boundary. Figure 6.3 shows a cross section of an example .vtk file, illustrating how the grid points are typically distributed when following this procedure for a model with a plume.

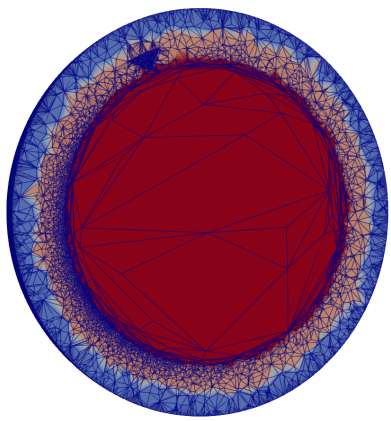

Figure 6.3: Cross section of an example `.vtk` file generated for a Ganymede model including a localised plume. The figure illustrates the typical distribution of grid points used by LIME when applying the random-weighted grid sampling approach. Higher grid point density is present near regions of strong gradients, such as the plume and the sub-solar area, ensuring accurate radiative transfer calculations in these zones.

Below the atmosphere (i.e., from the surface and inward), the grid cells were assigned physical properties chosen to ensure that the emission is optically thick and reproduces the surface temperature of Ganymede. In particular, the density was set to $3.3 \times 10^{22}\,\mathrm{cm}^{-3}$ (approximately 1 g/cm^3, similar to liquid water), the abundance to 10^{-10}, and the gas-to-dust ratio to 10^{-70}. With these values, the interior of Ganymede is effectively treated as a solid-sphere blackbody emitter at the local surface temperature. This setup has been verified to accurately reproduce the expected surface emission in test simulations. As a consequence, surface and subsurface properties such as reflectivity or dielectric effects are not taken into account in this model.

Implementing a water plume: Parametric Structure and Numerical Issues

A water plume is expected to have quite a complex shape and density distribution, but for this study I created a simplified 3D model to simulate its potential signature in SWI observations. The model simply assumes a homogeneous, conical jet of water vapor emitted from a circular vent from Ganymede's surface, which was implemented into LIME through the following sequential steps:

1. Creating a 3D Plume in Cartesian Space

The first step was to define the conical shape of the plume correctly in 3D space within the LIME code, so that the gas physical properties inside the plume could be set independently from other regions of the model.

Since it is not known if there will be a water plume on Ganymede and where it will be situated with respect to the subsolar point, I made the choice to create a cone whose position relative to the SSP can be parametrised using a rotation angle around the x-axis of the model. Since JUICE/SWI mostly will orbit in the equatorial plane of the Jupiter system, the observer position is instead parametrised with a rotation angle from the SSP around the z-axis (corresponding to the phase angle). This separation of rotation axes makes it possible to simulate and study different orientations of the plume and the spacecraft respectively, see Figure 6.4.

2. Analytical Description of Density and Temperature in the Plume

Once the geometry of the conical plume is defined, the second step was to express the density inside the plume in terms of a set of physical parameters which are more meaningful in describing and comparing water plumes:

- the water production rate Q in s^{-1},
- the circular vent radius r_{vent} in m,
- the exit radial velocity v_{exit} in $\mathrm{m\,s}^{-1}$,
- the gas kinetic temperature T_{plume} in K,
- the geometric factor f, defined as the height of the cone over the radius of the plume.

These parameters are used to determine both the volume and an estimate of the number of water molecules in the cone, assuming homogeneous conditions. In particular, the plume height h_{plume} in m is estimated by applying energy conservation for particles expanding radially from the surface with velocity v_{tot}:

$$h_{\mathrm{plume}} = \frac{v_{\mathrm{tot}}^2}{2g_{\mathrm{GAN}}} \tag{6.1}$$

where g_{GAN} is the surface gravity of Ganymede in $\mathrm{m\,s}^{-2}$. Given this geometry, the volume of the conical plume is calculated as:

$$V_{\mathrm{plume}} = \frac{1}{3}\pi\frac{h_{\mathrm{plume}}^3}{f^2} \tag{6.2}$$

Assuming particle energy conservation and that no water molecules escape the plume, the number density of water molecules in the plume can be approximated as::

$$n_{\mathrm{H_2O,plume}} = \frac{Q \cdot 2t}{V_{\mathrm{plume}}} \tag{6.3}$$

where Q is the water production rate in $\mathrm{mol\,s}^{-1}$, and $2t$ is the characteristic lifetime of the plume.

From Eq. 6.3 we can see that increasing the production rate or reducing the volume (e.g., through a smaller f) results in a higher number density, which in turn might affect the intensity of observed water signatures from the plume

in our radiative transfer simulations. A more detailed discussion of this aspect can be found in Section 2.3 of the paper attached to this thesis.

3. Structuring the Model into Six Distinct Regions

The third step was to implement different analytical functions for the physical properties in the plume as compared to the submlimation-dominated atmosphere, and the rest of the model volume. In order to achieve this, I divided the model volume into six different regions, each characterized by different physical properties in terms of density and temperature, see Figure 1 in Paper I. The main difficulty was not so much in the theoretical definition of the regions, but in their correct implementation within the code. Since LIME does not provide a direct interface to visualize the defined geometry, I used Paraview software to visually verify the proper spatial construction of each region. This required multiple iterations, adjustments, and careful attention to detail to guarantee that each area matched the desired physical conditions. This allowed me to ensure that the regions were well defined and free of overlaps or gaps.

The final step was the testing phase. When visualizing the model in ParaView, I noticed errors in the outer region of the model, where the water density should be extremely low. After multiple tests, I found that the molecular density which is given multiplying the number density and the abundance of the gas in this region should not be less of 10^{-25} to avoid problems with the gridding or ray-tracing steps in LIME. This required some tuning of the density and abundance values in this region to keep the model stable and working correctly.

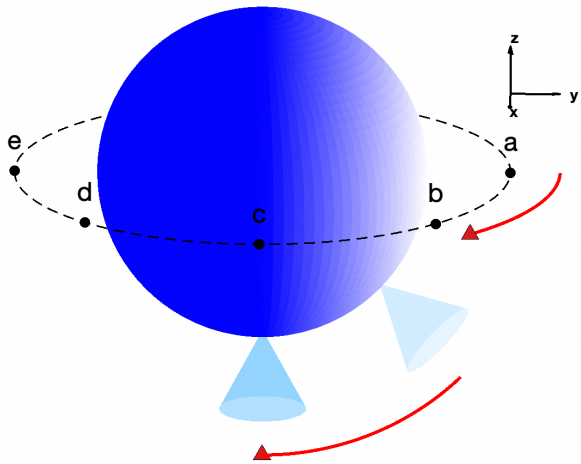

Figure 6.4: Illustration of Ganymede and SWI viewing geometry. Note that the sizes of Ganymede, the water plumes, and the SWI orbit are not to scale. This visualization was generated in MATLAB, with Ganymede modeled as a sphere illuminated according to the subsolar point (SSP), water plumes as cones, and the spacecraft orbit as a circular trajectory in the equatorial plane. SWI moves along the orbit from point **a** to **e**, corresponding to phase angles from 0° (nadir view at **a**) to 180° (**e**) in 45° steps; the red arrow along the orbit shows the direction of rotation around the z-axis. The primary plume is here positioned 90° from the SSP. To illustrate plume rotation around the x-axis, a second semi-transparent plume is shown at 45°; the curved red arrow indicates the direction of this rotation.

CHAPTER 7

Summary of Included Paper

This chapter provides a concise summary of Paper I, which forms the foundation of this thesis. In this study, we assess the feasibility of detecting water plumes in Ganymede's tenuous atmosphere using the Submillimeter Wave Instrument (SWI) onboard the JUICE mission, focusing on the 557.936 GHz ortho-H_2O line transition. We employed the LIME software package, a 3D non-LTE radiative transfer code, to simulate and analyse the spectral signatures of water plumes for different viewing geometries, considering an observing distance of approximately 1.2×10^6 km from Ganymede, corresponding to the planned moon monitoring phase of SWI. Key plume parameters – including temperature, production rate, and velocity fields – were modeled to investigate their influence on spectral features and assess the conditions under which SWI can detect plumes. These simulations are important for optimizing observational strategies and identifying the most favorable scenarios for plume detection.

Main Results of Paper I

- **Plume detectability from large distances:** The Submillimeter Wave Instrument (SWI) onboard JUICE can detect water plumes with production rates as low as 10^{27} s^{-1} from a distance of approximately 1.2 million km, provided favorable observational conditions. This demonstrates that plumes could be detected by SWI already during its moon monitoring campaign (see Chapter 3.2).

- **Optimal observing geometries:** Plume detection is significantly enhanced when the plume is located at the limb of Ganymede or positioned away from the SSP, which increases the contrast with the background. In these configurations, the plume introduces distinctive emission line wings – absent in no-plume models – with brightness temperature differences reaching up to $\sim$4 K.

- **Influence of plume temperature and production rate:** Increasing the water production rate from 10^{27} to 10^{30} s^{-1} results in only a moderate increase in emission intensity (less than 1 K), due to the high optical depth of the plume. In contrast, higher gas temperatures (e.g., 300 K compared to a typical 150 K plume) significantly enhance the spectral signal, increasing line wing emission by 10–20 K.

- **Spectral diagnostics of gas dynamics:** The velocity field within the plume affects both the shape and position of the spectral line. Radial velocities (e.g., 500 m/s) cause Doppler shifts, while broader thermal or turbulent velocity distributions lead to extended line wings. These features may serve as useful diagnostics for plume identification and dynamics.

- **SWI sensitivity and integration time:** A 10-minute integration using the high-resolution SWI mode can enable detection of modeled brightness temperature differences in favourabe scenarios, of $\sim$4 K, at a signal-to-noise ratio (SNR) of 7.

CHAPTER 8

Future Work

The results presented in Paper I suggest that SWI could potentially detect water plumes on Ganymede under favorable conditions during the moon-monitoring phase. At the same time, several limitations of the current model highlight possible directions for future work.

One aspect concerns the physical properties of the plume. In this study, we assumed a kinetic temperature of the plume of 150 K and also tested a higher value of 300 K, but these assumptions remain poorly constrained. Simulations and previous Direct Simulation Monte Carlo (DSMC) plume models of Europa by Tseng et al. (2022) indicate that the plume temperature drops rapidly from the initially assumed value to around 30-50 K as a result of adiabatic expansion to higher altitudes. Such conditions will affect the energy level populations and, consequently, the observed line strengths. A lower plume temperature might plausibly cause the H_2O line to appear in absorption in the plume core, although this also depends on the non-LTE effects (Cordiner et al., 2024). Future work will therefore include the analysis of low-temperature scenarios to assess their impact on SWI observations.

Our current plume model assumes a static, uniform, conical structure, suitable for an initial test of SWI's ability to detect plumes from about

1.2×10^6 km. A more realistic approach would introduce gradients in temperature, density, and velocity, as well as possible asymmetric venting or turbulence that can further complicate the structure of the plume. While such complexity is not critical for modeling the distant observations considered here, it will become necessary if plumes are detected and then observed from closer distances during JUICE moon flybys or from orbit around Ganymede. In that case, advanced plume simulations, for example using DSMC models, should be employed to capture more realistic shape and gradients in density, temperature and velocity.

Another aspect that requires attention is the extension of the parameter space. Our simulations focused on a single observing distance ($\sim 1.2 \times 10^6$ km) and on the 557.936 GHz ortho-water line. Further studies should investigate additional water transitions – in particular the para-water line transition at 1113 GHz ($1_{11} \rightarrow 0_{00}$), which will often be observed simultaneously with the 557 GHz line, see Figure 4.3. The atmospheric model can also be refined by incorporating collisional excitation by other collision partners such as H_2, O_2, atomic hydrogen (H), atomic oxygen (O), and electrons. However, for water, rates are only available for collisional excitation by H_2, H atoms and electrons (Daniel et al., 2011; Daniel et al., 2014; Faure et al., 2004), while O_2 could in fact be the dominating collision partner in most of the atmosphere (see Fig 2.2).

Furthermore, incorporating updated and more complete sets of collisional rate coefficients is expected to influence the non-LTE excitation in Ganymede's atmosphere, so would enhance the accuracy of water line modeling. For example, Mandal et al. (2023) has published updated H_2O:H_2O collision rates where many more transitions are included, which will be important in particular for modeling para-water transitions. Finally, similar models could also be extended to the other icy moons that will be targeted by JUICE, Europa and Callisto, enabling comparative studies and maximizing the scientific return of the mission.

References

Anderson, J. D., R. A. Jacobson, T. P. McElrath, W. B. Moore, G. Schubert, and P. C. Thomas (2001). "Shape, Mean Radius, Gravity Field, and Interior Structure of Callisto". In: *Icarus* 153.1, pp. 157–161. ISSN: 0019-1035. DOI: 10.1006/icar.2001.6664. URL: https://www.sciencedirect.com/science/article/pii/S0019103501966643.

Anderson, J. D., E. L. Lau, W. L. Sjogren, G. Schubert, and W. B. Moore (Dec. 1996). "Gravitational constraints on the internal structure of Ganymede". In: 384.6609, pp. 541–543. DOI: 10.1038/384541a0.

Barth, C. A., C. W. Hord, A. I. F. Stewart, W. R. Pryor, K. E. Simmons, W. E. McClintock, J. M. Ajello, K. L. Naviaux, and J. J. Aiello (Sept. 1997). "Galileo ultraviolet spectrometer observations of atomic hydrogen in the atmosphere of Ganymede". In: *Geophysical Research Letters* 24.17, pp. 2147–2150. DOI: 10.1029/97GL01927.

Bennacer, Yannis, Olivier Mousis, Marc Monnereau, Vincent Hue, and Antoine Schneeberger (June 2025). "Conditions for Accretion Favoring an Unmelted Callisto and a Differentiated Ganymede". In: 6.6, 138, p. 138. DOI: 10.3847/PSJ/add719. arXiv: 2505.07785 [astro-ph.EP].

Bockelée-Morvan, D., E. Lellouch, O. Poch, E. Quirico, S. Cazaux, I. de Pater, T. Fouchet, P. M. Fry, P. Rodriguez-Ovalle, F. Tosi, M. H. Wong, I. Boshuizen, K. de Kleer, L. N. Fletcher, L. Meunier, A. Mura, L. Roth, J. Saur, B. Schmitt, S. K. Trumbo, M. E. Brown, J. O'Donoghue, G. S. Orton, and M. R. Showalter (2024). "Composition and thermal properties of Ganymede's surface from JWST/NIRSpec and MIRI observations". In: *Astronomy & Astrophysics* 681, A27. DOI: 10.1051/0004-6361/202347326.

Brinch, C. and M. R. Hogerheijde (2010). "LIME - a flexible, non-LTE line excitation and radiation transfer method for millimeter and far-infrared wavelengths". In: 523, A25. DOI: 10.1051/0004-6361/201015333. arXiv: 1008.1492 [astro-ph.SR].

Buffa, G., O. Tarrini, F. Scappini, and C. Cecchi-Pestellini (2000). "H_2O-H_2O Collision Rate Coefficients". In: 128, pp. 597–601. DOI: 10.1086/313389.

Cavalié, Thibault and JUICE/SWI science team (Mar. 4, 2021). *SWI Observation Mode Library*. Issue JUI-MPS-SWI-OD-002. JUICE/SWI Operations Document.

Chen, G. A. et al. (Feb. 2014). "Tidal heating in icy satellite oceans". In: 229, pp. 11–30. DOI: 10.1016/j.icarus.2013.10.024.

Christner, B. C. et al. (2006). "Bacterial recovery from Antarctic subglacial ice and implications for life on Europa". In: *Nature* 441, pp. 453–456. DOI: 10.1038/nature04704.

Comrie, Angus, Kuo-Song Wang, Shou-Chieh Hsu, Anthony Moraghan, Pamela Harris, Qi Pang, Adrianna Pińska, Cheng-Chin Chiang, Rob Simmonds, Tien-Hao Chang, Hengtai Jan, and Ming-Yi Lin (Mar. 2021). *CARTA: Cube Analysis and Rendering Tool for Astronomy*. Astrophysics Source Code Library, record ascl:2103.031.

Connerney, J. E. P. et al. (2017). "The Juno Magnetic Field Investigation". In: *Space Science Reviews* 213 (November 2017), pp. 39–138. DOI: 10.1007/s11214-017-0334-z. URL: https://doi.org/10.1007/s11214-017-0334-z.

Cordiner, M. A., A. E. Thelen, I.-L. Lai, W.-L. Tseng, C. A. Nixon, Y.-J. Kuan, G. L. Villanueva, L. Paganini, S. B. Charnley, and K. D. Retherford (Apr. 2024). "ALMA Spectroscopy of Europa: A Search for Active Plumes". In: *arXiv e-prints*, arXiv:2404.05525, arXiv:2404.05525. DOI: 10.48550/arXiv.2404.05525. arXiv: 2404.05525 [astro-ph.EP].

Daniel, F., M.-L. Dubernet, and A. Grosjean (Dec. 2011). "Rotational excitation of 45 levels of ortho/para-H_2O by excited ortho/para-H_2 from 5 K to 1500 K: state-to-state, effective, and thermalized rate coefficients". In: *Astronomy & Astrophysics* 536, A76. DOI: 10.1051/0004-6361/201118049. URL: http://dx.doi.org/10.1051/0004-6361/201118049.

Daniel, F., A. Faure, P. J. Dagdigian, M.-L. Dubernet, F. Lique, and G. Pineau des Forêts (Nov. 2014). "Collisional excitation of water by hydrogen atoms". In: *Monthly Notices of the Royal Astronomical Society* 446.3, pp. 2312–2316.

DOI: 10.1093/mnras/stu2287. URL: http://dx.doi.org/10.1093/mnras/stu2287.

Dishoeck, Ewine F. van (2013). "Interstellar Water Chemistry: From Laboratory to Observations". In: *Chemical Reviews* 113.11, pp. 9043–9085. DOI: 10.1021/cr4003177.

Einstein, Albert (1917). "Zur Quantentheorie der Strahlung". In: *Physikalische Zeitschrift* 18. Received March 3, 1917; published March 15, 1917, pp. 121–128.

ESA (2012). *JUICE – JUpiter ICy moons Explorer*. https://www.esa.int/Science_Exploration/Space_Science/Juice. Accessed: 2025-08-20.

– (2023a). *ESA's JUICE lifts off on quest to discover secrets of Jupiter's icy moons*. https://www.esa.int/Science_Exploration/Space_Science/Juice/ESA_s_Juice_lifts_off_on_quest_to_discover_secrets_of_Jupiter_s_icy_moons. Accessed: 2025-08-20.

– (2023b). *JUICE Instruments*. URL: https://sci.esa.int/web/juice/-/61110-juice-instruments (visited on 08/20/2025).

– (2023c). *JUICE Mission Calendar*. https://www.cosmos.esa.int/web/juice/mission-calendar. Accessed: 2025-08-20.

– (2023d). *JUICE Payload*. URL: https://www.cosmos.esa.int/web/juice/payload (visited on 08/20/2025).

– (2023e). *SWI instrument*. URL: https://sci.esa.int/web/juice/-/61110-juice-instruments (visited on 08/20/2025).

Faure, Alexandre, Jimena D. Gorfinkiel, and Jonathan Tennyson (Jan. 2004). "Electron-impact rotational excitation of water". In: *Monthly Notices of the Royal Astronomical Society* 347.1, pp. 323–333. DOI: 10.1111/j.1365-2966.2004.07209.x. URL: http://dx.doi.org/10.1111/j.1365-2966.2004.07209.x.

Feldman, P. D., M. A. McGrath, D. F. Strobel, H. W. Moos, K. D. Retherford, and B. C. Wolven (June 2000). "HST/STIS Ultraviolet Imaging of Polar Aurora on Ganymede". In: 535, pp. 1085–1090. DOI: 10.1086/308889.

Gordy, Walter and Robert L. Cook (1984). *Microwave Molecular Spectra*. 3rd. Vol. 18. Techniques of Chemistry. Disponibile su https://archive.org/details/microwavemolecul0000gord. Wiley-Interscience. ISBN: 9780471086819.

Gurnett, D. A., W. S. Kurth, A. Roux, S. J. Bolton, and C. F. Kennel (Dec. 1996). "Evidence for a magnetosphere at Ganymede from plasma-wave ob-

servations by the Galileo spacecraft". In: 384.6609, pp. 535–537. DOI: 10.1038/384535a0.

Hall, D. T., P. D. Feldman, M. A. McGrath, and D. F. Strobel (May 1998). "The Far-Ultraviolet Oxygen Airglow of Europa and Ganymede". In: *The Astrophysical Journal* 499.1, pp. 475–481. DOI: 10.1086/305604.

Hansen, Candice J., Larry W. Esposito, A. Ian F. Stewart, Joshua E. Colwell, Amanda R. Hendrix, Wayne R. Pryor, Donald E. Shemansky, and Robert A. West (Mar. 2006). "Enceladus' Water Vapor Plume". In: *Science* 311.5766, pp. 1422–1425. DOI: 10.1126/science.1121254.

Hansen, G. B. and T. B. McCord (Jan. 2004). "Amorphous and crystalline ice on the Galilean satellites: A balance between thermal and radiolytic processes". In: *Journal of Geophysical Research: Planets* 109.E1. DOI: 10.1029/2003JE002149.

Hollas, J. Michael (1998). *Modern Spectroscopy*. 4th. Disponibile su https://www.amazon.com/Modern-Spectroscopy-J-Michael-Hollas/dp/0470844167. Wiley. ISBN: 9780470844168.

Hsu, H. et al. (2015). "Cassini's discovery of water vapor plumes on Enceladus". In: *Science* 349, pp. 282–285. DOI: 10.1126/science.aaa3007.

Jia, Xianzhe, Margaret G. Kivelson, Krishan K. Khurana, and William S. Kurth (June 2018). "Evidence of a plume on Europa from Galileo magnetic and plasma wave signatures". In: *Nature Astronomy* 2, pp. 459–464. DOI: 10.1038/s41550-018-0450-z.

Khurana, K. K., M. G. Kivelson, D. J. Stevenson, G. Schubert, C. T. Russell, R. J. Walker, and C. Polanskey (Oct. 1998). "Induced magnetic fields as evidence for subsurface oceans in Europa and Callisto". In: 395.6704, pp. 777–780. DOI: 10.1038/27394.

Kivelson, M. G., K. K. Khurana, C. T. Russell, R. J. Walker, C. Polanskey, G. Schubert, D. A. Gurnett, et al. (2000). "Europa's ocean and its potential for life". In: *Science* 289, pp. 1541–1545. DOI: 10.1126/science.289.5484.1541.

– (2002a). "Galileo magnetometer measurements: a stronger case for a subsurface ocean at Europa". In: *Science* 289, pp. 1340–1343. DOI: 10.1126/science.289.5483.1340.

Kivelson, M. G., K. K. Khurana, C. T. Russell, R. J. Walker, J. Warnecke, F. V. Coroniti, C. Polanskey, D. J. Southwood, and G. Schubert (Dec.

1996). "Discovery of Ganymede's magnetic field by the Galileo spacecraft". In: 384.6609, pp. 537–541. DOI: 10.1038/384537a0.

Kivelson, M. G., K. K. Khurana, and M. Volwerk (June 2002b). "The Permanent and Inductive Magnetic Moments of Ganymede". In: 157, pp. 507–522. DOI: 10.1006/icar.2002.6834.

Kleer, K. de, Z. Milby, C. Schmidt, M. Camarca, and M. E. Brown (Feb. 2023). "The Optical Aurorae of Europa, Ganymede, and Callisto". In: 4, p. 37. DOI: 10.3847/PSJ/acb53c. arXiv: 2302.08487 [astro-ph.EP].

Lari, G., M. Saillenfest, and M. Fenucci (July 2020). "Long-term evolution of the Galilean satellites: the capture of Callisto into resonance". In: 639, A40, A40. DOI: 10.1051/0004-6361/202037445. arXiv: 2001.01106 [astro-ph.EP].

Leblanc, F., A. V. Oza, L. Leclercq, C. Schmidt, T. Cassidy, R. Modolo, J.-Y. Chaufray, and R. E. Johnson (2017). "On the orbital variability of Ganymede's atmosphere". In: *Icarus* 293, pp. 185–198. DOI: 10.1016/j.icarus.2017.04.025. arXiv: 1804.10592 [astro-ph.EP]. URL: https://doi.org/10.1016/j.icarus.2017.04.025.

Ligier, N., C. Paranicas, J. Carter, F. Poulet, W. M. Calvin, T. A. Nordheim, C. Snodgrass, and L. Ferellec (Nov. 2019). "Surface composition and properties of Ganymede: Updates from ground-based observations with the near-infrared imaging spectrometer SINFONI/VLT/ESO". In: 333, pp. 496–515. DOI: 10.1016/j.icarus.2019.06.013. arXiv: 1910.07445 [astro-ph.EP].

Mandal, B. and D. Babikov (Mar. 2023). "Rate coefficients for rotational state-to-state transitions in H_2O + H_2O collisions for cometary and planetary applications, as predicted by mixed quantum-classical theory". In: 671, A51, A51. DOI: 10.1051/0004-6361/202245699.

Marconi, M. L. (Sept. 2007). "A kinetic model of Ganymede's atmosphere". In: 190, pp. 155–174. DOI: 10.1016/j.icarus.2007.02.016.

McGrath, M. A., E. Lellouch, D. F. Strobel, P. D. Feldman, and R. E. Johnson (2007). "Satellite Atmospheres". In: *Jupiter*. Ed. by F. Bagenal, T. E. Dowling, and W. B. McKinnon. Cambridge University Press, p. 457.

Meier, R. R. et al. (1992). "The role of ammonia and methanol in the subsurface oceans of icy moons". In: *Geophysical Research Letters* 19, pp. 2317–2320. DOI: 10.1029/92GL02627.

Mihalas, D. (1978). *Stellar Atmospheres*. San Francisco: W.H. Freeman.

Moore, W. B. and G. Schubert (2003). "The tidal response of Ganymede and Callisto with and without liquid water oceans". In: *Icarus* 166, pp. 223–226. DOI: 10.1016/j.icarus.2003.07.001.

Neufeld, D. A. and G. J. Melnick (1995). "Radiative Cooling of Dense Molecular Gas". In: *The Astrophysical Journal Supplement Series* 100.1, pp. 132–157. DOI: 10.1086/192083.

Nisini, B., M. Benedettini, T. Giannini, P. E. Clegg, A. M. Di Giorgio, R. Liseau, D. Lorenzetti, P. Saraceno, H. A. Smith, L. Spinoglio, and G. J. White (1999). "Strong H_2O and high-J CO emission towards the Class 0 protostar L1448-mm". In: *Astronomy & Astrophysics* 360, pp. 297–310.

Ojakangas, G. W. and D. J. Stevenson (1989). "Thermal evolution of icy satellites: Implications for subsurface oceans on Europa and Ganymede". In: *Icarus* 78, pp. 314–334. DOI: 10.1016/0019-1035(89)90069-5.

Orton, G. S., J. R. Spencer, L. D. Travis, T. Z. Martin, and L. K. Tamppari (Oct. 1996). "Galileo Photopolarimeter-Radiometer Observations of Jupiter and the Galilean Satellites". In: *Science* 274.5286, pp. 389–391. DOI: 10.1126/science.274.5286.389.

Paganini, L., G. L. Villanueva, L. Roth, A. M. Mandell, T. A. Hurford, K. D. Retherford, and M. J. Mumma (2019). "A measurement of water vapour amid a largely quiescent environment on Europa". In: *Nature Astronomy*. DOI: 10.1038/s41550-019-0933-6. URL: https://doi.org/10.1038/s41550-019-0933-6.

Pappalardo, R. T., J. W. Head, and R. Greeley (Oct. 1999). "The Hidden Ocean of Europa". In: *Scientific American* 281.4, pp. 54–63. DOI: 10.1038/scientificamerican1099-54.

Pence, W. D., L. Chiappetti, C. G. Page, R. A. Shaw, and E. Stobie (2010). "Definition of the Flexible Image Transport System (FITS), version 3.0". In: *Astronomy & Astrophysics* 524, A42. DOI: 10.1051/0004-6361/201015362.

Pilcher, C. B., S. T. Ridgway, and T. B. McCord (Dec. 1972). "Galilean Satellites: Identification of Water Frost". In: *Science* 178.4065, pp. 1087–1089. DOI: 10.1126/science.178.4065.1087.

Plainaki, C., S. Massetti, X. Jia, A. Mura, A. Milillo, D. Grassi, G. Sindoni, E. D'Aversa, and G. Filacchione (Sept. 2020). "Kinetic Simulations of the Jovian Energetic Ion Circulation around Ganymede". In: *Astrophysical Journal* 900.1, p. 74. DOI: 10.3847/1538-4357/aba94c.

Plainaki, C., A. Milillo, S. Massetti, A. Mura, X. Jia, S. Orsini, V. Mangano, E. De Angelis, and R. Rispoli (Jan. 2015). "The H_2O and O_2 exospheres of Ganymede: The result of a complex interaction between the jovian magnetospheric ions and the icy moon". In: *Icarus* 245, pp. 306–319. DOI: 10.1016/j.icarus.2014.09.018.

Poppe, A. R., S. Fatemi, and K. K. Khurana (June 2018). "Thermal and Energetic Ion Dynamics in Ganymede's Magnetosphere". In: *Journal of Geophysical Research: Space Physics* 123.6, pp. 4614–4637. DOI: 10.1029/2018JA025312.

Postberg, F., S. Kempf, J. Schmidt, N. Brilliantov, A. Beinsen, B. Abel, U. Buck, and R. Srama (2009). "The composition of Enceladus' plumes". In: *Nature* 459, pp. 1098–1101. DOI: 10.1038/nature08046.

Priscu, J. C., B. C. Christner, C. M. Foreman, R. Y. Morita, W. B. Lyons, and M. Tranter (2003). "Life in Lake Vostok: A unique Antarctic ecosystem". In: *Science* 302, pp. 2087–2090. DOI: 10.1126/science.1089220.

Ridley, J., K. Hand, C. Chyba, and V. Parro (2014). "Chemosynthetic microbes and their relevance to life on Europa". In: *Astrobiology* 14, pp. 168–174. DOI: 10.1089/ast.2013.1145.

Rohlfs, Kristen and Thomas L. Wilson (2004). *Tools of Radio Astronomy*. 4th ed. Astronomy and Astrophysics Library. Springer. ISBN: 978-3-662-05394-2. DOI: 10.1007/978-3-662-05394-2. URL: https://link.springer.com/book/10.1007/978-3-662-05394-2.

Roth, L., N. Ivchenko, G. R. Gladstone, J. Saur, D. Grodent, B. Bonfond, P. M. Molyneux, and K. D. Retherford (Oct. 2021). "A sublimated water atmosphere on Ganymede detected from Hubble Space Telescope observations". In: *Nature Astronomy* 5, pp. 1043–1051. DOI: 10.1038/s41550-021-01426-9. eprint: 2106.03570.

Roth, L., J. Saur, K. D. Retherford, D. F. Strobel, P. D. Feldman, M. A. McGrath, and F. Nimmo (2014a). "Hubble Space Telescope observations of Europa's water plumes". In: *Nature* 505, pp. 69–72. DOI: 10.1038/nature12873.

– (Jan. 2014b). "Transient Water Vapor at Europa's South Pole". In: *Science* 343, pp. 171–174. DOI: 10.1126/science.1247051.

Saur, Joachim, Stefan Duling, Lorenz Roth, Xianzhe Jia, Darrell F. Strobel, Paul D. Feldman, Ulrich R. Christensen, Kurt D. Retherford, Melissa A. McGrath, Fabrizio Musacchio, Alexandre Wennmacher, Fritz M. Neubauer,

Sven Simon, and Oliver Hartkorn (Mar. 2015). "The search for a subsurface ocean in Ganymede with Hubble Space Telescope observations of its auroral ovals". In: *Journal of Geophysical Research: Space Physics* 120.3, pp. 1715–1737. DOI: 10.1002/2014JA020778.

Saur, Joachim, Stefan Duling, Alexandre Wennmacher, Clarissa Willmes, Lorenz Roth, Darrell F. Strobel, Frédéric Allegrini, Fran Bagenal, Scott J. Bolton, Bertrand Bonfond, George Clark, Randy Gladstone, Thomas K. Greathouse, Denis C. Grodent, Candice J. Hansen, William S. Kurth, Glenn S. Orton, Kurt D. Retherford, Abigail M. Rymer, and Ali H. Sulaiman (Dec. 2022). "Alternating North-South Brightness Ratio of Ganymede's Auroral Ovals: Hubble Space Telescope Observations Around the Juno PJ34 Flyby". In: *Geophysical Research Letters* 49.23, e2022GL098600, e2022GL098600. DOI: 10.1029/2022GL098600. arXiv: 2208.09057 [astro-ph.EP].

Schroeder, Will, Ken Martin, and Bill Lorensen (2006). *The Visualization Toolkit: An Object-Oriented Approach to 3D Graphics*. 4th. Kitware, Inc. ISBN: 9781930934191.

Schubert, G., J. D. Anderson, T. Spohn, and W. B. McKinnon (2004). "Interior composition, structure and dynamics of the Galilean satellites". In: *Jupiter. The Planet, Satellites and Magnetosphere*. Ed. by Fran Bagenal, Timothy E. Dowling, and William B. McKinnon. Vol. 1, pp. 281–306.

Showman, Adam P., R. Malhotra, et al. (May 1997). "Tidal Evolution into the Laplace Resonance and the Resurfacing of Ganymede". In: *Icarus* 127.1, pp. 93–111. DOI: 10.1006/icar.1996.5669.

Showman, Adam P. and R. Malhotra (Oct. 1999). "The Galilean satellites". In: *Science* 286.5437, pp. 77–84. DOI: 10.1126/science.286.5437.77.

Siegert, Martin J., Michael C. Kennicutt, Robert A. Bindschadler, et al. (2001). "Subglacial lakes of Antarctica: Characteristics, processes and dynamics". In: *Nature* 409, pp. 411–416. DOI: 10.1038/35053069.

Sparks, William B., Kevin P. Hand, Melissa A. McGrath, Eric Bergeron, Michael Cracraft, and Susana E. Deustua (Oct. 2016). "Probing for Evidence of Plumes on Europa with HST/STIS". In: *The Astrophysical Journal* 829.2, 121, p. 121. DOI: 10.3847/0004-637X/829/2/121.

Spencer, John R. (Apr. 1987). "Icy Galilean satellite reflectance spectra - Less ice on Ganymede and Callisto?" In: *Icarus* 70, pp. 99–110. DOI: 10.1016/0019-1035(87)90077-7.

Spencer, John R., Francis Nimmo, et al. (2006). "Tidal heating of Enceladus and implications for the internal ocean". In: *Icarus* 182, pp. 198–203. DOI: 10.1016/j.icarus.2005.12.014.

Tinner, Chantal, André Galli, Fiona Bär, Antoine Pommerol, Martin Rubin, Audrey Vorburger, and Peter Wurz (Dec. 2024). "Electron-Induced Radiolysis of Water Ice and the Buildup of Oxygen". In: *Journal of Geophysical Research: Planets* 129.12, 2024JE008393. DOI: 10.1029/2024JE008393. arXiv: 2412.04079 [astro-ph.EP].

Tosi, Federico, Thomas Roatsch, André Galli, Ernst Hauber, Alice Lucchetti, Philippa Molyneux, Katrin Stephan, Nicholas Achilleos, Francesca Bovolo, John Carter, Thibault Cavalié, Giuseppe Cimò, Emiliano D'Aversa, Klaus Gwinner, Paul Hartogh, Hans Huybrighs, Yves Langevin, Emmanuel Lellouch, Alessandra Migliorini, Pasquale Palumbo, Giuseppe Piccioni, Jeffrey J. Plaut, Frank Postberg, François Poulet, Kurt Retherford, Ladislav Rezac, Lorenz Roth, Anezina Solomonidou, Gabriel Tobie, Paolo Tortora, Cecilia Tubiana, Roland Wagner, Eva Wirström, Peter Wurz, Francesca Zambon, Marco Zannoni, Stas Barabash, Lorenzo Bruzzone, Michele Dougherty, Randy Gladstone, Leonid I. Gurvits, Hauke Hussmann, Luciano Iess, Jan-Erik Wahlund, Olivier Witasse, Claire Vallat, and Rosario Lorente (Aug. 2024). "Characterization of the Surfaces and Near-Surface Atmospheres of Ganymede, Europa and Callisto by JUICE". In: *Space Science Reviews* 220.5, 59, p. 59. DOI: 10.1007/s11214-024-01089-8.

Trumbo, Samantha K., Michael E. Brown, Dominique Bockelée-Morvan, Imke de Pater, Thierry Fouchet, Michael H. Wong, Stéphanie Cazaux, Leigh N. Fletcher, Katherine de Kleer, Emmanuel Lellouch, Alessandro Mura, Olivier Poch, Eric Quirico, Pablo Rodriguez-Ovalle, Mark R. Showalter, Matthew S. Tiscareno, and Federico Tosi (July 2023). "Hydrogen peroxide at the poles of Ganymede". In: *Science Advances* 9.29, eadg3724, eadg3724. DOI: 10.1126/sciadv.adg3724.

Tseng, Wei-Ling, Ian-Lin Lai, Wing-Huen Ip, Hsiang-Wen Hsu, and Jong-Shinn Wu (2022). "The 3D Direct Simulation Monte Carlo Study of Europa's Gas Plume". In: *Universe* 8.5, p. 261. DOI: 10.3390/universe8050261.

Turc, L., L. Leclercq, F. Leblanc, R. Modolo, and J.-Y. Chaufray (May 2014). "Modelling Ganymede's neutral environment: A 3D test-particle simulation". In: *Icarus* 229, pp. 157–169. DOI: 10.1016/j.icarus.2013.11.005.

Van Hoolst, T. et al. (2024). “Geophysical Characterization of the Interiors of Ganymede, Callisto and Europa by ESA’s JUpiter ICy moons Explorer”. In: *Space Science Reviews* 220. DOI: 10.1007/s11214-024-01085-y. URL: https://doi.org/10.1007/s11214-024-01085-y.

Vance, Steven D., Mark P. Panning, Simon Stähler, Fabio Cammarano, Bruce G. Bills, Gabriel Tobie, Shunichi Kamata, Sharon Kedar, Christophe Sotin, William T. Pike, Ralph Lorenz, Hsin-Hua Huang, Jennifer M. Jackson, and Bruce Banerdt (Jan. 2018). “Geophysical Investigations of Habitability in Ice-Covered Ocean Worlds”. In: *Journal of Geophysical Research: Planets* 123.1, pp. 180–205. DOI: 10.1002/2017JE005341. arXiv: 1705.03999 [astro-ph.EP].

Vorburger, Audrey, Shahab Fatemi, André Galli, Lucas Liuzzo, Andrew R. Poppe, and Peter Wurz (Mar. 2022). “3D Monte-Carlo simulation of Ganymede’s water exosphere”. In: *Icarus* 375, 114810, p. 114810. DOI: 10.1016/j.icarus.2021.114810.

Waite, J. Hunter, Michael R. Combi, Wing-Huen Ip, Thomas E. Cravens, Ralph L. McNutt, Wayne Kasprzak, Roger Yelle, Janet Luhmann, Hasso Niemann, David Gell, Brian Magee, Greg Fletcher, Jonathan Lunine, and Wei-Ling Tseng (Mar. 2006). “Cassini Ion and Neutral Mass Spectrometer: Enceladus Plume Composition and Structure”. In: *Science* 311.5766, 1419, pp. 1419–1422. DOI: 10.1126/science.1121290.

Wirström, E. S., P. Bjerkeli, L. Rezac, C. Brinch, and P. Hartogh (May 2020). “Effect of the 3D distribution on water observations made with the SWI. I. Ganymede”. In: *Astronomy Astrophysics* 637, A90, A90. DOI: 10.1051/0004-6361/202037609.

Yamamoto, Takeshi O. (2017). “High-resolution spectroscopy of the "ΣN cusp"”. In: *Journal of Molecular Spectroscopy* 13. Disponibile su https://iopscience.iop.org/article/10.1088/1674-1056/13/2/020007, p. 020007. DOI: 10.1088/1674-1056/13/2/020007.

Yung, Y. L. and M. B. McElroy (Jan. 1977). “Stability of an Oxygen Atmosphere on Ganymede”. In: *Icarus* 30.1, pp. 97–103. DOI: 10.1016/0019-1035(77)90124-5.

Zimmer, C. et al. (2000). “Subsurface Oceans on Europa and Callisto: Constraints from Galileo Magnetometer Observations”. In: *Icarus* 147.1, pp. 282–289. DOI: 10.1006/icar.2000.6456.